Monthly Notices
of the
ROYAL ASTRONOMICAL SOCIETY

Mon. Not. R. Astron. Soc. **415,** 1827–1848 (2011) doi:10.1111/j.1365-2966.2011.18832.x

Population study for γ-ray pulsars with the outer-gap model – III. Radiation characteristics and viewing geometry

J. Takata,[⋆] Y. Wang[⋆] and K. S. Cheng[⋆]
Department of Physics, University of Hong Kong, Pokfulam Road, Hong Kong, China

Accepted 2011 March 29. Received 2011 March 28; in original form 2011 February 25

ABSTRACT

We have performed a Monte Carlo simulation of the Galactic population of pulsars and γ-ray observations. We apply a two-layer outer-gap model, which has been developed by Wang, Takata & Cheng, of the γ-ray emission process, and study the radiation characteristics as a function of the magnetic inclination angle (α) and the Earth viewing angle (ζ). In our model, the γ-ray flux and the spectral cut-off energy tend to decrease as the inclination and viewing angles deviate from 90°. The emerging spectrum above 100 MeV becomes soft with a photon index $p \sim 1.8$–2 for $\zeta \rightarrow 90^{\circ}$ and $p \sim 1.2$–1.3 for $\zeta \ll 90^{\circ}$. Our simulation predicts that pulsars with larger inclination angles ($\alpha = 70$–90°) and larger viewing angles ($\zeta = 70$–90°) have been preferentially detected by the *Fermi* γ-ray telescope, and hence the observed pulse profiles of the γ-ray pulsars have a double-peak structure rather than a single-peak one. In the simulation, most γ-ray millisecond pulsars are categorized as radio-quiet γ-ray pulsars, because their radio fluxes are under the sensitivities of the major radio surveys. Even if we drastically increase the radio sensitivity by a factor of 10, the number of radio-selected millisecond pulsars detected by *Fermi* 10-year observations is still much lower than the expected number of γ-ray-selected millisecond pulsars, indicating that radio-quiet millisecond pulsars must contribute to *Fermi* unidentified sources and/or γ-ray background radiation. We argue that γ-ray pulsars observed with a smaller viewing angle ($\zeta \ll 90^{\circ}$) will appear as low-efficiency γ-ray pulsars. For example, the unique radiation properties of the low-efficiency γ-ray pulsar PSR J0659+1414 can be explained by our present gap model with a viewing geometry of $\alpha \sim \zeta = 40^{\circ}$–$50^{\circ}$.

Key words: radiation mechanisms: non-thermal – methods: statistical – stars: neutron – pulsars: general – gamma-rays: stars.

1 INTRODUCTION

The Large Area Telescope (LAT) on board the *Fermi* γ-ray telescope has increased the number of known γ-ray pulsars and the recent *Fermi* catalogue includes more than 60 γ-ray pulsars, including 9 millisecond pulsars (Abdo et al. 2009a,b, 2010a;[1] Saz Parkinson et al. 2010). Furthermore, the detection of radio millisecond pulsars associated with about 20 unidentified *Fermi* point sources (e.g. Caraveo 2010; Keith et al. 2011; Ransom et al. 2011; Ray & Saz Parkinson 2011) has been reported, suggesting that millisecond pulsars, as well as canonical pulsars, constitute one of the major Galactic γ-ray sources. It is expected that more γ-ray pulsars will be added to the list over the course of the *Fermi* mission. The spectral shape and pulse morphology measured by *Fermi* have been used to discriminate between particle acceleration and γ-ray emission models: the polar-cap model (Ruderman & Sutherland 1975; Daugherty & Harding 1982, 1996), the slot-gap model (Arons 1983; Muslimov & Harding 2004; Harding et al. 2008; Harding & Muslimov 2011) and the outer-gap model (Cheng, Ho & Ruderman 1986a,b; Hirotani 2008; Takata, Wang & Cheng 2010a). The polar-cap model assumes an acceleration region near the stellar surface, and the slot-gap and outer-gap models assume an emission region extending to the outer magnetosphere. The cut-off features of the γ-ray spectra of the Crab and Vela pulsars measured by *Fermi* imply that the γ-ray emission site of canonical pulsars is located in the outer magnetosphere rather than near the polar-cap region, which produces a cut-off feature steeper than the observed one (Aliu et al. 2008; Abdo et al. 2009c, 2010d). Romani & Watters (2010) and Watters & Romani (2011) have studied the morphology of the pulse profiles of young pulsars predicted by outer-gap and slot-gap models, and they argued statistically that the outer-gap geometry is more consistent with the *Fermi* observations

---

⋆E-mail: takata@hku.hk (JT); yuwang@hku.hk (YW); hrspksc@hkucc.hku.hk (KSC)

[1] See also http://fermi.gsfc.nasa.gov/ssc/data/access/lat/1yr_catalog/.

than the slot-gap model. Venter, Harding & Guillemot (2009) found that the observed pulse profiles of several millisecond pulsars detected by *Fermi* cannot be explained by the outer-gap and/or slot-gap models, and proposed a pair-starved polar-cap model in which the particles are continuously accelerated up to high altitude because of insufficient multiplicity of the pairs.

The high-quality data measured by *Fermi* enable us to perform a detailed study of the population of γ-ray pulsars. Takata et al. (2010a) have studied the relation between the emission properties (luminosity and spectral cut-off energy) and pulsar characteristics (e.g. rotation period and magnetic field). They proposed that the outer-gap accelerator model controlled by the magnetic pair-creation process can explain the observed population statistics better than a model controlled by the photon–photon pair-creation process (Zhang & Cheng 1997, 2003). Wang, Takata & Cheng (2010) have fitted the observed phase-averaged spectra by using a two-layer outer-gap model, in which the accelerator consists of a wide but low-charge-density main region and a narrow but high-charge-density screening region. They suggested that the relation between the γ-ray luminosity (L_γ) and the spin-down power ($L_{\rm sd}$) can be expressed as $L_\gamma \propto L_{\rm sd}^{\beta}$ with $\beta \sim 0$ for $L_{\rm sd} \geq 10^{36}\,{\rm erg\,s^{-1}}$, while $\beta \sim 0.5$ for $L_{\rm sd} \leq 10^{36}\,{\rm erg\,s^{-1}}$. This relation is consistent with the theoretical expectation, i.e. the gap fractional size f is determined by $f = \min(f_{\rm zc}, f_{\rm m})$, where $f_{\rm zc}$ and $f_{\rm m}$ are the gap size determined by photon–photon (Zhang & Cheng 1997, 2003) and magnetic (Takata et al. 2010a) pair-creation processes, respectively (cf. Section 3.2). Equating $f_{\rm zc}$ and $f_{\rm m}$ corresponds to $L_{\rm sd} \sim 10^{36}\,{\rm erg\,s^{-1}}$.

The study of the population synthesis of radio pulsars has been developed using detailed modelling of the radio emission and radio surveys (e.g. Bailes & Kniffen 1992; Sturner & Dermer 1996; Faucher-Giguère & Kaspi 2006). Also population studies of γ-ray pulsars have been developed by several authors (e.g. Gonthier et al. 2002 for the polar-cap model, Cheng & Zhang 1998 for the outer-gap model and Story, Gonthier & Harding 2007 for the slot-gap model). For example, Story et al. (2007) studied the population of γ-ray millisecond pulsars with the slot-gap accelerator model and predicted the *Fermi* observations. They predicted that *Fermi* will detect 12 radio-loud and 33–40 radio-quiet γ-ray millisecond pulsars. Using Monte Carlo simulations of the outer gap, Takata, Wang & Cheng (2011a,b) have explained the observed distributions of characteristics of the γ-ray pulsars detected by *Fermi* with six-month long observations. They predicted that at least 80 γ-ray canonical pulsars should have a γ-ray flux exceeding the sensitivity of the six-month *Fermi* observations, suggesting that the present observations have missed many γ-ray-emitting pulsars. Watters & Romani (2011) simulated the Galactic distribution of the young γ-ray pulsars and compared the simulated pulse morphology with the *Fermi* results. They argued statistically that the outer-gap model explains the distributions of the pulse morphology (e.g. the phase separation of the two peaks) measured by *Fermi* better than the slot-gap model. Population studies (e.g. Kaaret & Cottam 1996; Faucher-Giguère & Loeb 2010; Takata et al. 2011b) have also pointed out that unidentified pulsars, in particular millisecond pulsars located at high Galactic latitudes, will be associated with *Fermi* unidentified sources (Abdo et al. 2010b) and will contribute to the γ-ray background radiation.

In the our previous studies (Takata et al. 2011a,b), we ignored the dependence of the radiation characteristics on the viewing geometry (i.e. the magnetic inclination angle and the Earth viewing angle measured from the pulsar's rotation axis) and focused on the distributions of the properties (e.g. rotation period and magnetic field) of γ-ray pulsars. However, the observed radiation characteristics, such as the flux, spectral cut-off energy and pulse profile, must be affected by the viewing geometry. To perform a more solid study of the population, which is compared with high-quality *Fermi* data, a three-dimensional model that takes into account the dependence of the radiation characteristics on the viewing geometry is required.

In this paper, we develop a Monte Carlo study for the population of γ-ray pulsars with a radiation model that takes into account the dependence on viewing geometry. In Section 2, we review the Monte Carlo simulation for the population of γ-ray pulsars. We discuss our outer-gap model in Section 3. In Section 4.1, we discuss the dependence of the radiation characteristics on the viewing geometry. In Section 4.2, we compare the results of the Monte Carlo simulation with *Fermi* six-month long observations. We also show the expected population of γ-ray pulsars if the *Fermi* observations continue for five years or ten years. In Section 5, after summarizing our simulation results, we discuss the viewing geometry of PSR J0659+1414, which is known as a low-efficiency γ-ray pulsar.

2 MONTE CARLO SIMULATION FOR THE PULSAR POPULATION

In this paper, we denote canonical pulsars and millisecond pulsars as CPs and MSPs, respectively. We assume that the birth rates of CPs and MSPs are $\sim 10^{-2}\,{\rm yr^{-1}}$ and $\sim 10^{-6}$–$10^{-5}\,{\rm yr^{-1}}$ (Lorimer et al. 1995; Lorimer 2008), respectively, and we ignore the millisecond pulsars in globular clusters. The birth location is determined by the spatial distributions given by (Paczynski 1990)

$$\rho_R(R) = \frac{a_R {\rm e}^{-R/R_{\rm exp}} R}{R_{\rm exp}^2},$$
$$\rho_Z(Z) = \frac{1}{Z_{\rm exp}} {\rm e}^{-|Z|/Z_{\rm exp}}, \qquad (1)$$

where R is the axial distance from the axis through the Galactic centre perpendicular to the Galactic disc and Z is the distance from the Galactic disc, $R_{\rm exp} = 4.5\,{\rm kpc}$ and $a_R = [1 - {\rm e}^{-R_{\rm max}/R_{\rm exp}}(1 + R_{\rm max}/R_{\rm exp})]^{-1}$ with $R_{\rm max} = 20\,{\rm kpc}$. In addition, we apply $Z_{\rm exp} = 75\,{\rm pc}$ for CPs and $Z_{\rm exp} = 200\,{\rm pc}$ for MSPs, respectively.

To obtain the current position of each simulated pulsar, we solve the equation of motion from its birth to the current time. The equation of motion is given by

$$\frac{{\rm d}R^2}{{\rm d}t^2} = \frac{v_\phi^2}{R} - \frac{\partial \Phi_{\rm tot}}{\partial R}, \qquad (2)$$

$$\frac{\mathrm{d}Z^2}{\mathrm{d}t^2} = -\frac{\partial \Phi_{\mathrm{tot}}}{\partial Z} \tag{3}$$

and

$$R v_\phi = \mathrm{constant}. \tag{4}$$

Here v_ϕ is the azimuthal component of the velocity and $\Phi_{\mathrm{tot}} = \Phi_{\mathrm{sph}} + \Phi_{\mathrm{dis}} + \Phi_{\mathrm{h}}$ is the total gravitational potential, where Φ_{sph}, Φ_{dis} and Φ_{h} are spheroidal, disc and halo components of the Galactic gravitational potential and are given by

$$\Phi_i(R, Z) = -\frac{G M_i}{\sqrt{R^2 + [a_i + (Z^2 + b_i^2)^{1/2}]^2}}, \tag{5}$$

where i = sph and dis, $a_{\mathrm{sph}} = 0$, $b_{\mathrm{sph}} = 0.277$ kpc, $M_{\mathrm{sph}} = 1.12 \times 10^{10}\,\mathrm{M}_\odot$, $a_{\mathrm{dis}} = 3.7$ kpc, $b_{\mathrm{dis}} = 0.20$ kpc and $M_{\mathrm{dis}} = 8.07 \times 10^{10}\,\mathrm{M}_\odot$, while for the halo component

$$\Phi_{\mathrm{h}}(r) = -\frac{G M_{\mathrm{c}}}{r_{\mathrm{c}}} \left[\frac{1}{2} \ln\left(1 + \frac{r^2}{r_{\mathrm{c}}^2}\right) + \frac{r_{\mathrm{c}}}{r} \tan^{-1}\left(\frac{r}{r_{\mathrm{c}}}\right)\right], \tag{6}$$

where $r_{\mathrm{c}} = 6.0$ kpc and $M_{\mathrm{c}} = 5.0 \times 10^{10}\,\mathrm{M}_\odot$ (cf. Burton & Gordon 1978; Binney & Tremaine 1987; Paczynski 1990). The Lagrangian in units of energy per unit mass is given by

$$L = \frac{v^2(R, Z, \phi)}{2} - \Phi_{\mathrm{tot}}(R, Z), \tag{7}$$

where v is the velocity.

For the initial velocity of each modelled pulsar, we assume a random isotropic direction of the velocity and a magnitude drawn from a Maxwellian distribution with a characteristic width of $\sigma_V = 265\,\mathrm{km\,s^{-1}}$ for CPs and $\sigma_V = 70\,\mathrm{km\,s^{-1}}$ for MSPs (cf. Hobbs et al. 2005), namely

$$\rho_V(V) = \sqrt{\frac{\pi}{2}} \frac{V^2}{\sigma_V^3} \mathrm{e}^{-V^2/2\sigma_V^2}. \tag{8}$$

2.1 Pulsar characteristics

In this section, we describe how we calculate the current value of various characteristics of the simulated pulsars.

2.1.1 Canonical pulsars

For a canonical γ-ray pulsar, which is born soon after the supernova explosion, the true age is more or less equal to the spin-down age $\tau = P/2\dot{P}$, where P and $\dot{P}$ are the rotation period and its time derivative. This allows us to calculate the present distributions of the pulsar characteristics from the initial distributions.

For the Crab pulsar, the initial period is estimated to be $P_0 \sim 19$ ms. A short birth rotation period is also expected for the young 16-ms pulsar PSR J0537−0691 (Marshall et al. 1998), suggesting that most pulsars were born with $P_0 \sim$ 20–30 ms. There is good evidence that some pulsars were born with a longer initial period (e.g. $P_0 \sim 62$ ms for PSR J1911−1925: Kaspi et al. 2001). However, we found that the distribution of initial rotation period does not much affect the results of the following Monte Carlo simulation. For example, we compared the results of two simulations with different distributions of initial period; one has all simulated pulsars randomly distributed in the range P_0 = 20–30 ms and the other has 70 per cent of pulsars distributed in the range P_0 = 20–30 ms and 30 per cent in the range P_0 = 20–100 ms. In such a case, we could not see any significant difference in the populations of the simulated γ-ray pulsars. The difference in the simulated distributions of γ-ray pulsars becomes significant if we assume that >50 per cent of newborn pulsars are distributed with initial period $P_0 \geq$ 30 ms. Because we do not know the exact distribution of the initial period well, we randomly choose the initial period to be in the narrow range P_0 = 20–30 ms, which provides a more consistent result for our simulation for comparison with *Fermi* observations.

We assume a Gaussian distribution in $\log_{10} B_{\mathrm{s}}$ for the initial distribution of the stellar magnetic field measured at the magnetic equator,

$$\rho_B(\log_{10} B_{\mathrm{s}}) = \frac{1}{\sqrt{2\pi}\sigma_B} \exp\left[-\frac{1}{2}\left(\frac{\log_{10} B_{\mathrm{s}} - \log_{10} B_0}{\sigma_B}\right)^2\right]. \tag{9}$$

In this study, we apply $\log_{10} B_0 = 12.6$ and $\sigma_B = 0.1$. Because canonical γ-ray pulsars are younger than 10 Myr, we ignore the evolution of the stellar magnetic field, which may be important for neutron stars with age greater than 10 Myr (Goldreich & Reisenegger 1992; Hoyos, Reisenegger & Valdivia 2008).

With a constant stellar magnetic field in time, the period evolves as

$$P(t) = \left(P_0^2 + \frac{16\pi^2 R_{\mathrm{s}}^6 B_{\mathrm{s}}^2}{3 I c^3} t\right)^{1/2}, \tag{10}$$

where $R_{\mathrm{s}} = 10^6$ cm is the stellar surface and $I = 10^{45}\,\mathrm{g\,cm^2}$ is the neutron-star moment of inertia. In addition, we artificially assumed that the magnetic inclination angle does not evolve with spin-down age, while a decrease in the spin-down time-scale has been pointed out (e.g. Davis

& Goldstein 1970; Michel 1991; Tauris & Manchester 1998). The time derivative of the rotation period is calculated from

$$\dot{P}(t) = \frac{8\pi^2 R_s^6 B_s^2}{3Ic^3 P}. \tag{11}$$

2.1.2 *Millisecond pulsar*

We assume that all MSPs are born through the so-called recycled process, in which the accretion of matter from a low-mass companion star spins up the neutron star. It implies that the true age of the binary system is different from the spin-down age of the MSP. However, we expect that the Galactic distribution does not depend on the spin-down age of MSPs. With the typical velocity of observed MSPs, $V \sim 70\,\mathrm{km\,s^{-1}}$, it is expected that the displacement of MSPs (or binary systems) with typical age, $\geq$100 Myr, becomes larger than the size of the Galaxy. With a relatively slow velocity, $V \leq 100\,\mathrm{km\,s^{-1}}$, however, the MSPs remain bound in the Galactic potential and hence their Galactic distribution does not depend on spin-down age.

The initial rotation period of a MSP is related to the history of the accretion process after the decaying stage of the magnetic field (Campana et al. 1998; Takata, Cheng & Taam 2010b). However, the description of the transition from the accretion-powered to the rotation-powered phase is not well understood due to complexities in the description of the interaction between the magnetosphere of a neutron star and its accretion disc (Romanova et al. 2009). Furthermore, the true age of a MSP after the supernova explosion in a binary system is different from the spin-down age of that MSP. These theoretical uncertainties make it difficult to obtain the present distributions of MSP properties from the initial distributions.

In this paper, we assign 'current' pulsar properties for each simulated MSP, instead of modelling from the initial distributions: namely, we (1) randomly select the age of the simulated MSP up to 10 Gyr, (2) shift the simulated MSP from its birth location to the current location and (3) assign the parameters of the MSP following the observed distributions. We assign the period time derivative ($\dot{P}$) and stellar magnetic field (B_s) following the observed $\dot{P} - B_s$ distribution (Manchester et al. 2005). From the assigned period time derivative and the stellar magnetic field, the current rotation period and spin-down age are calculated from

$$P_{-3} = 0.97 B_8^2 \dot{P}_{-20}^{-1}\,\mathrm{ms} \tag{12}$$

and

$$\tau = 1.5 \times 10^9 P_{-3} \dot{P}_{20}^{-1}\,\mathrm{yr}, \tag{13}$$

respectively (Lyne & Graham-Smith 2006). Here B_8 is the stellar magnetic field in units of 10^8 G and P_{-3} and $\dot{P}_{-20}$ are the rotation period in units of 1 ms and its time derivative in units of 10^{-20}, respectively. In fact, the above process can provide a Galactic distribution of radio MSPs consistent with observations (cf. Takata et al. 2011b).

2.2 Radio emission

Using the empirical relation between radio luminosity, rotation period and period time derivative, the distribution of the radio luminosity at 400 MHz is expressed by (Narayan & Ostriker 1990)

$$\rho_{L_{400}} = 0.5\lambda^2 \mathrm{e}^{\lambda}, \tag{14}$$

where $\lambda = 3.6[\log_{10}(L_{400}/\langle L_{400}\rangle) + 1.8]$ with $\langle L_{400}\rangle = \eta 10^{6.64} \dot{P}^{1/3}/P^3$, and L_{400} is the luminosity in units of mJy kpc^2. Here η is a scaling factor to adjust the observed distribution and $\eta = 1$ (or 0.05) for CPs (or MSPs). The radio flux on Earth is given by $S_{400} = L_{400}/d^2$, where d is the distance to the pulsar. We scale the simulated 400-MHz luminosity to the observational frequency using a typical photon index of $\sim$2 for CPs and $\sim$1.8 for MSPs, respectively (Kramer et al. 1997, 1998).

We take into account the beaming of the radio emission. For CPs, we apply the half-angle, which is measured from the magnetic axis, of the radio cone studied by Kijak & Gil (1998, 2003):

$$\omega_{\mathrm{CP}} \sim 1\overset{\circ}{.}24 r_{\mathrm{KG}}^{1/2} P^{-1/2}, \tag{15}$$

where

$$r_{\mathrm{KG}} = 40 \nu_{\mathrm{GHz}}^{-0.26} \dot{P}_{-15}^{0.07} P^{0.3},$$

where $\dot{P}_{-15}$ is the period time derivative in units of 10^{-15} and ν_{GHz} is the radio frequency in units of GHz. For MSPs, the half-angle does not depend on the frequency and is approximately described as (Kramer & Xilouris 2000)

$$\omega_{\mathrm{MSP}} \sim \omega_0 (P/1\,\mathrm{s})^{-1/2}, \tag{16}$$

where ω_0 is randomly chosen in the range $2\overset{\circ}{.}75$–$5\overset{\circ}{.}4$. The radio emission can be detected by an observer with a viewing angle between max(0°, $\alpha - \omega_i$) and min($\alpha + \omega_i, 90^\circ$), where $i =$ CP or MSP and α is the inclination angle between the rotation axis and the magnetic axis.

We use the 10 radio surveys (Molongo 2, Green Band 2 and 3, Arecibo 2 and 3, Parkes 1, 2 and MB, Jordell Bank 2 and Swinburne IL) with system characteristics listed in table 1 of Takata et al. (2011a) and the references therein. To calculate the dispersion measure, we apply the Galactic distribution of electrons studied by Cordes & Lazio (2002).

3 γ-RAY EMISSION MODEL

Pulsar rotation energy, which is thought to be an essential energy source of γ-ray emission, can be released by both current braking torque and magnetic dipole radiation. According to the analysis of a force-free magnetosphere by Spitkovsky (2006), the spin-down power depends on the inclination angle as $L_{\rm sd} \propto 1 + \sin^2\alpha$; in other words, $L_{\rm sd}$ changes only by a factor of 2 with inclination angle. In the present Monte Carlo study, therefore, we ignore the dependence of the spin-down power on the inclination angle, and apply the conventional expression that $L_{\rm sd} = 4(2\pi)^4 B_{\rm s}^2 R_{\rm s}^6/6c^3P^4$.

3.1 Two-layer outer-gap model

The outer-gap dynamics is controlled by the pair-creation process, which produces a charge distribution in the transfield direction (Cheng et al. 1986a,b; Takata, Shibata & Hirotani 2004). Wang et al. (2010) and Wang, Takata & Cheng (2011) argued that the outer gap should be approximately divided into two layers, i.e. the main acceleration region starting from the last-open field lines and the screening region lying in the upper part of the gap. In the main acceleration region, the charge density is ∼10 per cent of the Goldreich–Julian value (Goldreich & Julian 1969) and a strong electric field accelerates electrons and positrons up to a Lorentz factor of $\Gamma \sim 10^{7.5}$. The accelerated particles emit several GeV photons via the curvature radiation process. In the screening region, the large number of pairs created by the pair-creation process starts to screen out the gap electric field. The curvature radiation from the screening pairs produces mainly ∼100 MeV photons.

A simple description of the electric field structure inside a two-layer outer gap is discussed in Wang et al. (2010, 2011). We denote x, z and ϕ as the coordinates along the magnetic field line, perpendicular to the magnetic field line in the poloidal plane and in the magnetic azimuth, respectively. We expect that the particle number density increases exponentially near the boundary ($z = h_1$) between the main acceleration and screening regions (Cheng et al. 1986a,b), and that the charge density is almost constant in the screening region (Hirotani 2006). Hence, we approximately describe the distribution of the charge density in the z-direction with the step function as follows:

$$\rho(\boldsymbol{r}) = \begin{cases} \rho_1(x,\phi), & \text{if} \quad 0 \le z \le h_1(x,\phi), \\ \rho_2(x,\phi), & \text{if} \quad h_1(x,\phi) < z \le h_2(x,\phi), \end{cases} \tag{17}$$

where, $|\rho_1| < |\rho_{\rm GJ}| < |\rho_2|$, $z = 0$ and $z = h_2$ correspond to the last-open field line and the upper boundary of the gap, respectively. For simplicity, we define the boundary between main acceleration region and the screening region, i.e. h_1, by a magnetic field line with an approximation such that h_1/h_2 is constant along the magnetic field line. The present model predicts that the charge density in the screening region should be proportional to the Goldreich–Julian charge density (Wang et al. 2010). This situation will be satisfied because there are many pairs created by the pair-creation process in the screening region. In the main acceleration region, because the number density is much smaller than the Goldreich–Julian value, its distribution along the magnetic field line is not important for the electric field distribution. Therefore, we approximate that $\rho - \rho_{\rm GJ} \sim g(z,\phi)\rho_{\rm GJ}(\boldsymbol{r})$ for both main acceleration and screening regions, where

$$g(z,\phi) = \begin{cases} -g_1(\phi), & \text{if} \quad 0 \le z \le h_1(x,\phi), \\ g_2(\phi), & \text{if} \quad h_1(x,\phi) < z \le h_2(x,\phi). \end{cases} \tag{18}$$

We assume that $g_1 > 0$ and $g_2 > 0$ so that $|\rho| < |\rho_{\rm GJ}|$ for the main acceleration region and $|\rho| > |\rho_{\rm GJ}|$ for the screening region.

To obtain the typical strength of the electric field in the gap, we find the solution of the Poisson equation for each azimuthal angle (cf. Wang et al. 2010, 2011):

$$\frac{\partial^2}{\partial z^2}\Phi'(x,z,\phi)|_{\phi=\rm fixed} = -4\pi[\rho(x,z,\phi) - \rho_{\rm GJ}(\boldsymbol{r})]_{\phi=\rm fixed}, \tag{19}$$

where Φ' is the electric potential of the accelerating field. Here we assume that the derivative of the potential field in the z-direction is much larger than that in the x-direction and the ϕ-direction.

In this paper, we neglect the z-dependence of the Goldreich–Julian charge density and approximate the Goldreich–Julian charge density as $\rho_{\rm GJ}(x,\phi) \sim -\Omega Bx/2\pi cR_{\rm c}$ (Cheng et al. 1986a,b), where Ω and $R_{\rm c}$ are the angular frequency of the pulsar and the curvature radius of the field line, respectively. The boundary conditions on the lower ($z = 0$) and upper ($z = h_2$) boundaries are given by

$$\Phi'(x, z=0, \phi) = 0 \quad \text{and} \quad \Phi'(x, z=h_2, \phi) = 0 \tag{20}$$

respectively. Imposing the condition that Φ' and $\partial\Phi'/\partial z$ are continuous at the boundary $z = h_1$, we obtain the solution as

$$\Phi'(\boldsymbol{r}) = -\frac{\Omega Bxh_2^2(x,\phi)}{cR_{\rm c}} \begin{cases} -g_1(\phi)z'^2 + C_1z', & \text{for} \quad 0 \le z' \le h_1(x,\phi)/h_2(x,\phi), \\ g_2(\phi)(z'^2-1) + D_1(z'-1), & \text{for} \quad h_1(x,\phi)/h_2(x,\phi) \le z' \le 1, \end{cases} \tag{21}$$

where

$$C_1(x,\phi) = -\frac{g_1h_1(h_1-2h_2) + g_2(h_1-h_2)^2}{h_2^2},$$

$$D_2(x,\phi) = -\frac{g_1h_1^2 + g_2h_2^2}{h_2^2}$$

and $z'\equiv z/h_2(x,\phi)$. The accelerating electric field, $E_{\parallel}=-\partial\Phi'/\partial x$, is written as

$$E_{||}(\boldsymbol{r})\sim\frac{\Omega B h_2^2(x,\phi)}{cR_{\rm s}}\begin{cases}-g_1(\phi)z'^2+C_1(\boldsymbol{r})z', & \text{for}\quad 0\leq z'\leq h_1(x,\phi)/h_2(x,\phi),\\ g_2(\phi)(z'^2-1)+D_1(\boldsymbol{r})(z'-1), & \text{for}\quad h_1(x,\phi)/h_2(x,\phi)<z'\leq 1,\end{cases}\tag{22}$$

where we used the dipole-field relations $\partial(Bh_2^2)/\partial x\sim 0$, $\partial z'/\partial x=\partial(z/h_2)/\partial x\sim 0$, $\partial(h_1/h_2)/\partial x\sim 0$ and approximated that $\partial R_{\rm c}/\partial x\sim 0$.

On the upper boundary, we anticipate that the total potential field (corotational potential + non-corotational potential) in the gap is continuously connected to the corotational potential field outside the gap. This screening condition is described by

$$\frac{\partial\Phi'}{\partial z}|_{z=h_2}=-E_{\perp}(x,z=h_2,\phi)=0.\tag{23}$$

This condition gives the relation between (h_1,h_2) and (g_1,g_2) as

$$\left(\frac{h_2}{h_1}\right)^2=1+\frac{g_1}{g_2}.\tag{24}$$

In this paper we do not consider the azimuthal distribution of the dimensionless charge density g_1 and g_2, because we discuss the general properties of the γ-ray emission. The azimuthal structure will be important for explaining detailed observed properties, such as the existing of the third peak in the pulse profile of the Vela pulsar measured by *Fermi* and the energy dependence of the pulse phase of the third peak (cf. Wang et al. 2011).

The typical Lorentz factor of the accelerated particles can be estimated by force balance between the electric field and the curvature radiation drag force as

$$\Gamma=\left(\frac{3R_{\rm c}^2}{2e}E_{||}\right)^{1/4}.\tag{25}$$

The spectrum of the curvature radiation emitted by the individual particle is written as

$$P_{\rm c}(E_\gamma,\boldsymbol{r})=\frac{\sqrt{3}e^2\Gamma}{hR_{\rm c}}F(\chi),\tag{26}$$

where $\chi=E_\gamma/E_{\rm c}$ with $E_{\rm c}=3hc\Gamma^3/4\pi R_{\rm c}$ and

$$F(\chi)=\chi\int_\chi^\infty K_{5/3}(\xi)\,{\rm d}\xi,$$

where $K_{5/3}$ is the modified Bessel function of order 5/3. A γ-ray spectrum measured on Earth may be expressed by (e.g. Hirotani 2008)

$$\frac{{\rm d}F_\gamma}{{\rm d}E_\gamma}\sim\frac{1}{d^2}\sum_{\boldsymbol{r}_i}N(\boldsymbol{r}_i)P_{\rm c}(E_\gamma,\boldsymbol{r}_i)R_{\rm c}(\boldsymbol{r}_i)\triangle A_i,\tag{27}$$

where $N\sim|\rho_{\rm GJ}|/e$ is the particle number density, $\boldsymbol{r}_i$ represents the radius to the emission point from which the emission is measured by the observer, $\triangle A_i$ is the area of the calculation grid perpendicular to the magnetic field lines. The integrated energy flux between 100 MeV and 300 GeV can be calculated from

$$F_{\gamma,100}=\int_{100\,{\rm MeV}}^{300\,{\rm GeV}}\frac{{\rm d}F_\gamma}{{\rm d}E_\gamma}\,{\rm d}E_\gamma.\tag{28}$$

In the gap, the curvature photons are emitted in the direction of the particle motion, which may be described as (Takata, Chang & Cheng 2007)

$$\boldsymbol{v}=v_{\rm p}\boldsymbol{B}/B+\boldsymbol{r}\times\boldsymbol{\Omega},\tag{29}$$

where the first term represents the motion along the magnetic field line, $v_{\rm p}$ is calculated from the condition that $|\boldsymbol{v}|=c$ and the second term is the corotation motion. The emission direction measured from the rotation axis (i.e. viewing angle) ζ and the pulse phase ψ are calculated from (Yadigaroglu 1997)

$$\begin{cases}\cos\zeta=\boldsymbol{n}\cdot\boldsymbol{e}_\Omega,\\ \psi=-\psi_n-\boldsymbol{r}/R_{\rm lc}\cdot\boldsymbol{n},\end{cases}\tag{30}$$

where $\boldsymbol{n}=\boldsymbol{v}/v$, $\boldsymbol{e}_\Omega$ is the unit vector in the direction of the rotation axis and ψ_n is the azimuthal angle of the emission direction.

3.2 Outer-gap geometry

In this paper, we adopt a rotating vacuum dipole field as the magnetosphere and assume that a strong emission region extends between the null charge surface ($\boldsymbol{\Omega}\cdot\boldsymbol{B}=0$) of the Goldreich–Julian charge density and the radial distance $r=R_{\rm lc}$, where $R_{\rm lc}=cP/2\pi$ is the light-cylinder radius. Electrodynamics studies have pointed out that the gap current can shift the inner boundary toward the stellar surface (e.g. Takata et al. 2004). However, because it is expected that the curvature radiation below the null charge surface appears with an emissivity much smaller than that above the null charge surface (e.g. Hirotani 2006), we ignore its contribution to the calculation.

We define the fractional gap thickness measured on the stellar surface as

$$f \equiv \frac{h_2(R_{\rm s},\phi)}{r_{\rm p}(\phi)}, \tag{31}$$

where $r_{\rm p}$ is the polar-cap radius. Note that, because the electric field $E_\parallel$ is proportional to Bh_2^2, it can be found that $E_\parallel \propto f^2$.

Zhang & Cheng (1997, 2003) have argued for a self-consistent outer-gap model controlled by the photon–photon pair-creation process between curvature photons and X-rays from the stellar surface. They estimated the gap fraction as

$$f_{\rm zc,\,CP} = \frac{h_2(R_{\rm s},\phi)}{r_{\rm p}(\phi)} \sim \frac{D_\perp(R_{\rm lc})}{R_{\rm lc}} = 5.5(P/1\,{\rm s})^{26/21}(B_{\rm s}/10^{12}\,{\rm G})^{-4/7} \tag{32}$$

for CPs and

$$f_{\rm zc,\,MSP} = 7.0\times10^{-2}(P/1\,{\rm ms})^{26/21}(B_{\rm s}/10^{8}\,{\rm G})^{-4/7}\delta r_5^{7/2} \tag{33}$$

for MSPs. Here $\delta\, r_5$ is the distance (in units of 10^5 cm) from the stellar surface to the position at which the local magnetic field is comparable to the dipole field, and it will take a value of $\delta\, r_5 \sim 1$–10.

We note that Zhang & Cheng (1997, 2003) estimated the gap fraction by a completely vacuum electric field $E_\parallel = \Omega Bf^2R_{\rm lc}^2/cR_{\rm c}$. With the same gap fraction, the solution described by equation (22) gives an electric field at least a factor of four smaller than that used in Zhang & Cheng (1997, 2003). This difference can be important for the typical energy of curvature radiation ($E_{\rm c}$), because $E_{\rm c} \propto E_\parallel^{3/4}$. In other words, if we derive the gap fraction from the pair-creation condition that $E_{\rm X}E_{\rm c} = (m_{\rm e}\, c^2)^2$, where $E_{\rm X}$ is the X-ray photon energy, the present model predicts a fractional gap thickness larger than that of Zhang & Cheng (1997, 2003). In this paper, reducing the electric field in the model of Zhang & Cheng (1997, 2003) by a factor of four, we find that the gap fraction is increased by a factor of $4^{3/7} \sim 1.8$ from the values in equations (32) and (33).

Takata et al. (2010a) proposed that the outer-gap model can be controlled by the magnetic pair-creation process taking place near the stellar surface. They argued that half of the particles created in the gap or injected into the outer gap at the outer boundary return to the stellar surface, and these returning particles emit ~100 MeV photons near the stellar surface. A good fraction of 100-MeV photons can make pairs through the magnetic pair-creation process. They argued that if the magnetic field lines near the surface, rather than nearly perpendicular to the surface, are bending sideways due to the strong local field, the pairs created in these local magnetic field lines can have a pitch angle defined by the angle between the directions of particle motion and the field line, smaller than 90°, which results in an outgoing flow of pairs; hence the pairs control the size of the outer gap. We also note that the outgoing flow may be produced by Compton scattering. With this model, the fractional gap thickness is estimated as

$$f_{\rm m} \sim \frac{D_\perp(R_{\rm s})}{R_{\rm p}} = 0.8K(P/1_{\rm s})^{1/2}, \tag{34}$$

where $K \sim B_{\rm m,12}^{-2}\, s_7$ is the parameter characterizing the local parameters, i.e. $B_{\rm m,12}$ and s_7, which are the local magnetic field in units of 10^{12} G and the local curvature radius in units of 10^7 cm, respectively. By fitting the emission characteristics of γ-ray pulsars observed by *Fermi*, Takata et al. (2010a) estimated $K \sim 2$ for CPs and $K \sim 15$ for MSPs. When the fractional gap thickness $f_{\rm m}$ is smaller (or larger) than $f_{\rm zc}$, the magnetic pair-creation (or photon–photon pair-creation) process controls the gap thickness.

We note that the outer gap should only exist between the last-open field lines and the critical magnetic field lines that have null charge points at the light cylinder. Fig. 1 shows the polar angle, measured from the magnetic axis, of the polar-cap rim ($\theta_{\rm p}$, solid line) and of footpoints of the critical field lines ($\theta_{\rm c}$, dashed line) as a function of the magnetic azimuth. The maximum gap fraction is defined by $f_{\rm max} = (\theta_{\rm p} - \theta_{\rm c})/\theta_{\rm p}$, and is represented by the dotted line in Fig. 1. The azimuthal angle $\phi = 0$ in Fig. 1 corresponds to the plane spanned by the rotation axis and the magnetic axis. In this paper, we anticipate that the azimuthal expansion of the active gap is limited as $f_{\rm zc,m} \le f_{\rm max}(\phi)$ and $-90^\circ \le \phi \le 90^\circ$.

4 RESULTS

In this paper, we present the results of the two-layer outer-gap model using a ratio of $h_1/h_2 = 0.95$ and a dimensionless charge density in the main region of $1 - g_1 = 0.3$. The value $h_1/h_2 = 0.95$ is chosen because Wang et al. (2010) fitted the phase-averaged spectra of mature pulsars by using $h_1/h_2 \sim 0.95$. The value $1 - g_1 = 0.3$ is slightly larger than the $1 - g_1 \sim 0.1$ used in Wang et al. (2010), but reproduces a simulated population more consistent with *Fermi* observations. The gap height h_2 and charge density in the screening region g_2 are calculated from equations (31) and (24), respectively.

4.1 Dependence on the inclination and viewing angles

The dependence of the characteristics of the calculated γ-ray spectra on the inclination angle and viewing angle are summarized in Figs 2–8. Fig. 2 shows the phase plot of photons having energies larger than 100 MeV. The result is for $\alpha = 60^\circ$, $B_{12} = 3\times10^{12}$ G and $f_{\rm zc} = 0.1$.

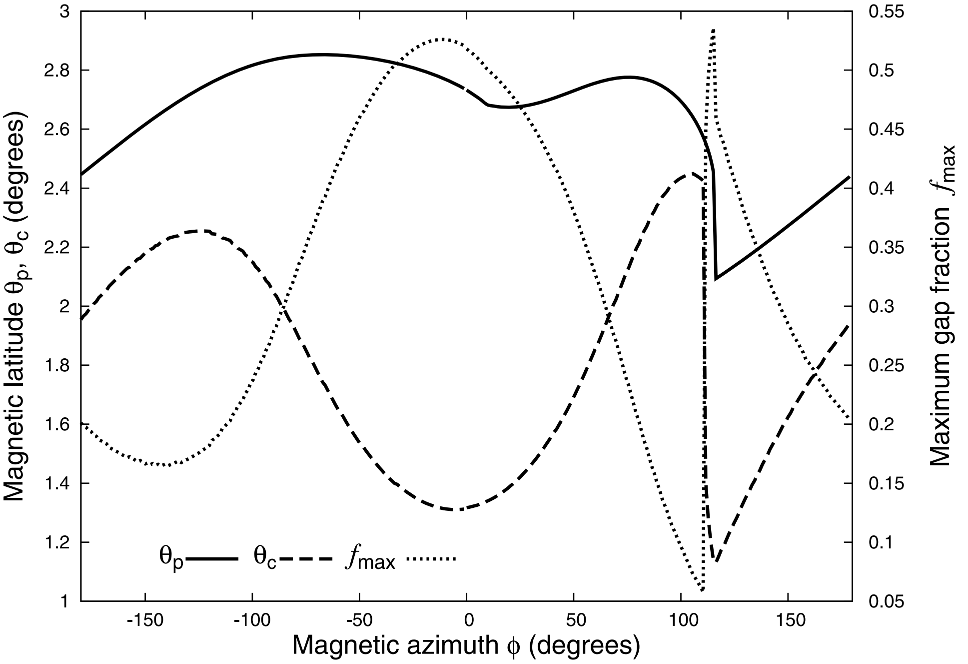

Figure 1. Latitudes of the polar-cap rim θ_{p} (solid line) and the critical magnetic field line θ_{c} (dashed line). The dotted line shows the maximum gap fraction $f_{\max} = (\theta_{\mathrm{p}} - \theta_{\mathrm{c}})/\theta_{\mathrm{p}}$. The magnetic azimuth $\phi = 0$ corresponds to the magnetic meridian, which includes the rotation and magnetic axes. The results are for inclination angle $\alpha = 45^{\circ}$ and rotation period $P = 0.1$ s.

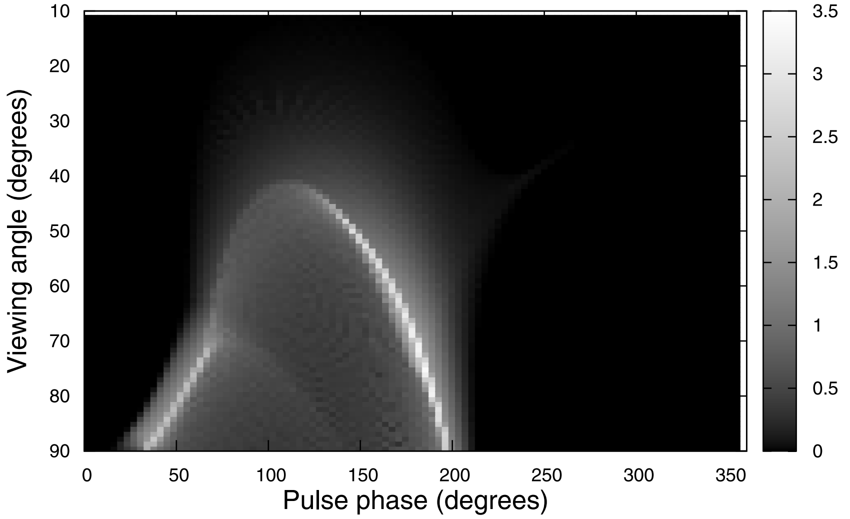

Figure 2. Phase plot of photons having energies larger than 100 MeV. The results are for $\alpha = 60^{\circ}$, $B = 3 \times 10^{12}$ G and $f_{\mathrm{zc}} = 0.1$.

4.1.1 γ-ray flux

The left panels in Figs 3 and 4 show the γ-ray flux ($\geq$100 MeV) as a function of the viewing angle ζ and inclination angle α. The vertical line (y axis) represents the fractional γ-ray flux, which is defined as the flux measured by $f^3 L_{\mathrm{sd}}/d^2$ (cf. Takata et al. 2011b). Here we calculated the rotation period using $B_{\mathrm{s}} = 3 \times 10^{12}$ G and gap fraction $f = f_{\mathrm{zc}}$. We can see that the calculated flux tends to decrease as the line of sight approaches the rotation axis, where $\zeta = 0^{\circ}$. In the sky map of Fig. 2, we see that large viewing angles ($\zeta \rightarrow 90^{\circ}$) encounter a more intense emission region, whereas small viewing angles ($\zeta \ll 90^{\circ}$) encounter a less intense region or even miss the emission region. With the outer-gap geometry running from the null charge surface to the light cylinder, an observer with a smaller viewing angle ($\zeta \ll 90^{\circ}$) may miss emission from higher latitudes ($z \geq h_2/2$) and measure only emission from the lower part of the gap ($z \sim 0$). Because the accelerating electric field vanishes at the lower boundary of the gap ($z = 0$), the Lorentz factor of the accelerated particles and the resultant emissivity of the curvature radiation around the lower boundary of the gap are significantly decreased. Consequently, a smaller viewing angle tends to measure a smaller flux of curvature radiation. In the left panels of Figs 3 and 4, we also see that the tendency for the fractional flux to decrease with decreasing viewing angle is more gradual for larger inclination angles. This is because the emission from an outer gap with larger inclination angle

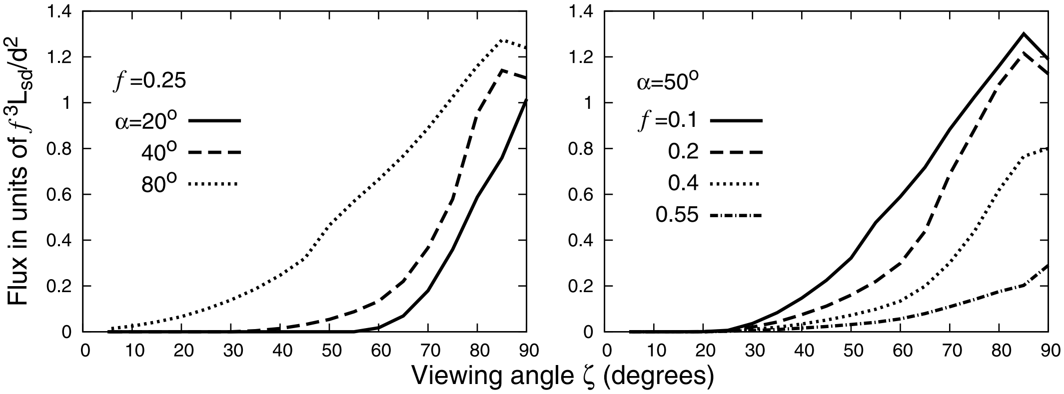

Figure 3. The γ-ray flux (>100 MeV) measured as a function of viewing angle. The results are for a canonical pulsar with $B_{\rm s} = 3 \times 10^{12}$ G and $f = f_{\rm zc}$. Left: the γ-ray flux for the inclination angle $\alpha = 20°$ (solid line), 40° (dashed line) and 80° (dotted line). The results are for a gap fraction of $f = 0.25$. Right: the γ-ray flux for $f = 0.1$ (solid line), 0.2 (dashed line), 0.4 (dotted line) and 0.55 (dash–dotted line). The results are for an inclination angle of $\alpha = 50°$.

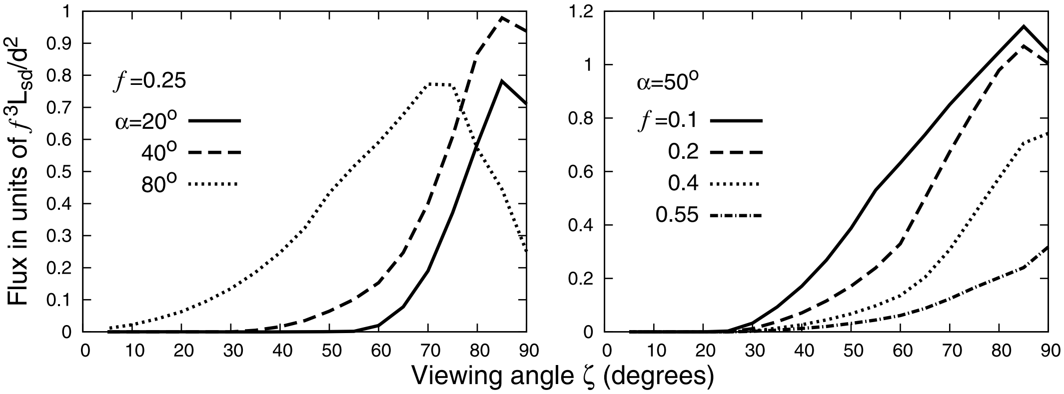

Figure 4. The same as Fig. 3, but for a millisecond pulsar with $B_{\rm s} = 3 \times 10^{8}$ G.

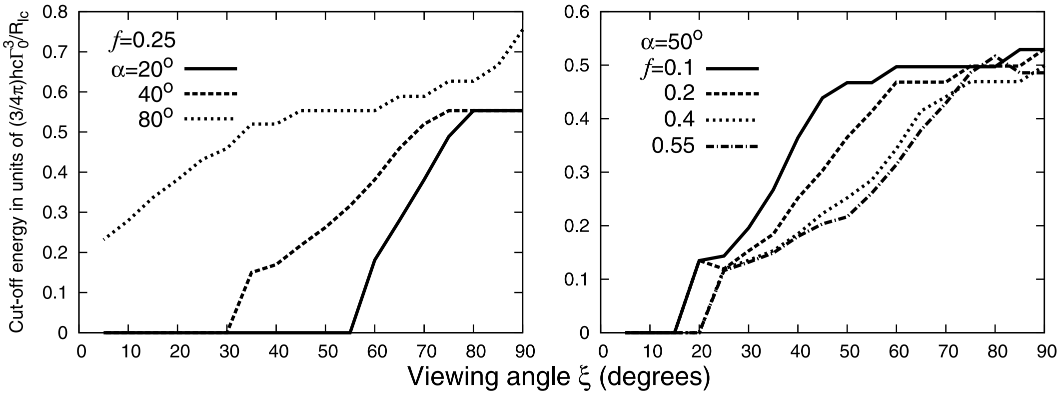

Figure 5. Dependence of spectral cut-off energy on the viewing geometry. The vertical line represents the cut-off energy in units of $(3/4\pi)hc\Gamma_0^3/R_{\rm lc}$, where $\Gamma_0 = (3R_{\rm lc}^2 E_{\parallel,0}/2e)^{1/4}$ with $E_{\parallel,0} = f^2 B(R_{\rm lc})$. The results are for a canonical pulsar with $B_{\rm s} = 3 \times 10^{12}$ G and $f = f_{\rm zc}$. The lines correspond to the same cases as Fig. 3.

covers a wider region of the sky. These dependences of the γ-ray flux on the viewing geometry predict that *Fermi* has preferentially detected pulsars with larger inclination angles and larger viewing angles near 90° (cf. Section 4.2.2).

The right panels in Figs 3 and 4 summarize the dependence of the fractional γ-ray flux on the gap fractional thickness. We can see that the fractional flux decreases as the gap fraction increases. This dependence is related to the expansion of the outer gap in the azimuthal direction. In the present calculation, we have assumed that the azimuthal expansion of the active gap is limited as $f \le f_{\rm max}(\phi)$ and $-90° \le \phi \le 90°$. As the dotted line in Fig. 1 shows, $f_{\rm max}$ acquires a maximum value near the magnetic meridian, where $\phi = 0°$, and tends to decrease as the azimuthal angle deviates from $\phi = 0$. This implies that the width of the active gap in the azimuthal direction narrows with the increase of gap fractional thickness, f. Consequently, the fractional flux tends to decrease as the gap fraction increases.

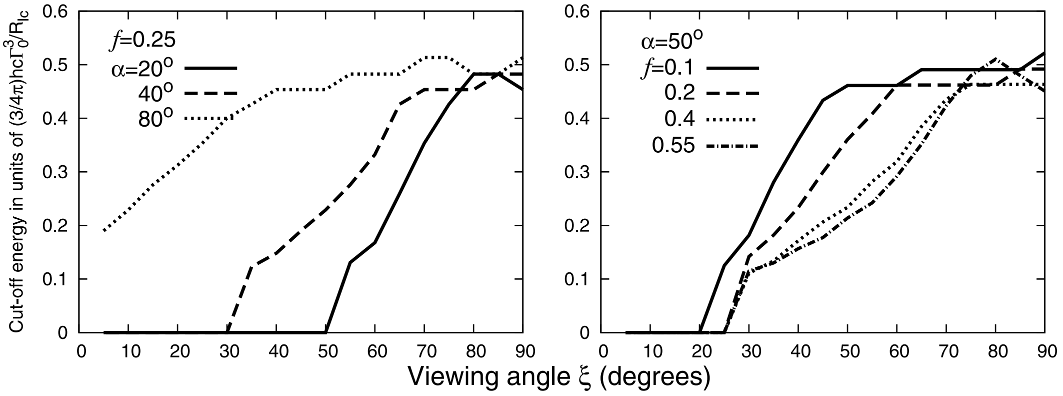

Figure 6. The same as Fig. 5, but for a millisecond pulsar with $B_s = 3 \times 10^8$ G.

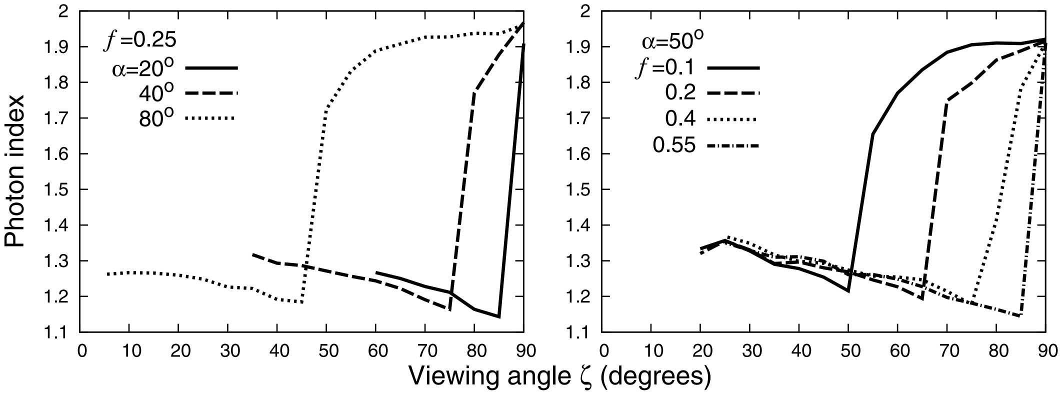

Figure 7. Dependence of photon index on the viewing geometry. The results are for a canonical pulsar with $B_s = 3 \times 10^{12}$ G. The lines correspond to the same cases as Fig. 3.

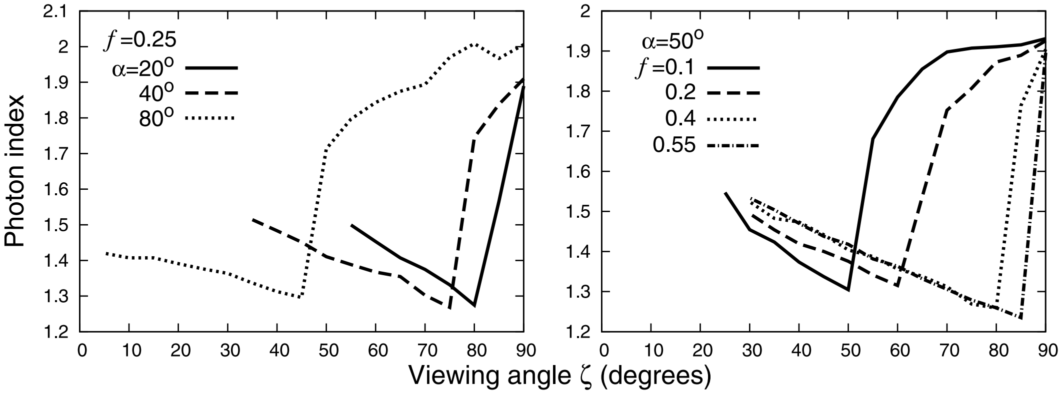

Figure 8. The same as Fig. 7, but for a millisecond pulsar with $B_s = 3 \times 10^8$ G and $f = f_{zc}$.

4.1.2 Cut-off energy

The cut-off energy is calculated as the peak energy in the spectral energy distribution of the emission from the main acceleration region. Figs 5 and 6 show the dependence of the cut-off energies of CPs and MSPs, respectively, on the viewing geometry. The vertical axis represents the cut-off energy measured by $3hc\Gamma_0^3/4\pi R_{\rm lc}$, where $\Gamma_0 = (3R_{\rm lc}^2 E_{\parallel,0}/2e)^{1/4}$ with $E_{\parallel,0} = f^2 B(R_{\rm lc})$. Figs 5 and 6 show that the cut-off energy decreases with decreasing viewing angle. As we argued in Section 4.1.1, an observer with a large viewing angle $\zeta \sim 90°$ can encounter emission from the strong accelerating electric field region in the middle of the gap ($z \sim h_2/2$), whereas an observer with a small viewing angle ($\zeta \ll 90°$) measures the emission from the small electric field region near the lower boundary ($z \sim 0$). As a result, the cut-off energy in the spectrum decreases with decreasing viewing angle. We also find in Figs 5 and 6 that the fractional cut-off energy does not depend much on the fractional gap thickness f.

4.1.3 Photon index

We applied the minimized χ^2 method to fit the spectrum between 100 MeV and the cut-off energy with a single power-law form. Figs 7 and 8 show the dependence of the photon index of CPs and MSPs, respectively, on the viewing geometry. Our model predicts that the spectral shape is relatively soft with a photon index $p \sim 1.8$–2 for larger viewing angles ($\zeta \rightarrow 90^\circ$) and hard with $p \sim 1.2$–1.3 for smaller viewing angles ($\zeta \ll 90^\circ$). In Figs 7 and 8, the transition from soft to hard spectra occurs within a narrow range of viewing angle. In the present two-layer model, the screening region and the main acceleration region produce γ-ray photons with a typical energy of ~100 MeV and ~1 GeV, respectively. For viewing angles closer to $\zeta \sim 90^\circ$, because the observed γ-ray radiation consists of emission from both main acceleration and screening regions, the emerging spectrum becomes soft with a photon index of $p \sim 1.8$–2 above 100 MeV. For smaller viewing angles, on the other hand, because the emission of the screening region is missing, only emission from the main acceleration region contributes to the spectrum. In such a case, the emerging spectrum has a photon index $p \sim 1.2$–1.3 above 100 MeV, which closes to a mono-energetic curvature spectrum.

4.2 Results of the Monte Carlo simulation

In this section we present the results of the Monte Carlo simulation, in which we assume that the birth rates of CPs and MSPs are ~0.015 and $\sim 9 \times 10^{-6}$ per year, respectively. We also assume that the viewing angle and inclination angle are randomly distributed. For inclination angles close to $\alpha \sim 90^\circ$, for which the null charge points are located on or very close to the stellar surface, a numerical error may occur when we search the last-open field lines of the rotating vacuum field. To avoid this, we limit ourselves to inclination angles below $\alpha \leq 85^\circ$. Because a comparison between simulated and observed distributions for the various properties (e.g. rotation period and magnetic field) of γ-ray pulsars was performed in Takata et al. (2011a,b), we focus on the characteristics of the γ-ray radiation with regards to the viewing geometry.

When considering the sensitivity of the observations, we refer to the *Fermi* first pulsar catalogue (Abdo et al. 2010a). For radio-selected pulsars, *Fermi* archived a sensitivity $F \sim 10^{-11}$ erg cm^{-2} s^{-1} (or $\sim 3 \times 10^{-11}$ erg cm^{-2} s^{-1}) for Galactic latitudes $|b| \geq 5^\circ$ (or $<5^\circ$) for six-month long observations. For CPs, the *Fermi* six-month data allow us to detect the pulsed period by a blind search, if the γ-ray flux is larger than $F \geq 2 \times 10^{-11}$ for $|b| \geq 5^\circ$ and $F \geq 6 \times 10^{-11}$ for $|b| \leq 5^\circ$. For MSPs, because there are no such detections of γ-ray-selected pulsars so far, we cannot simulate the *Fermi* sensitivity using a blind search. In this paper, therefore, we simulate the population of γ-ray-selected MSPs using the *Fermi* sensitivity for the blind search of CPs.

4.2.1 Viewing geometry

Figs 9 and 10 plot the inclination angle (α) and the viewing angle (ζ) of the 100 simulated canonical and millisecond γ-ray pulsars, respectively. Filled circles and boxes represent radio-selected and γ-ray-selected γ-ray pulsars, respectively. For CPs, we can see in Fig. 9

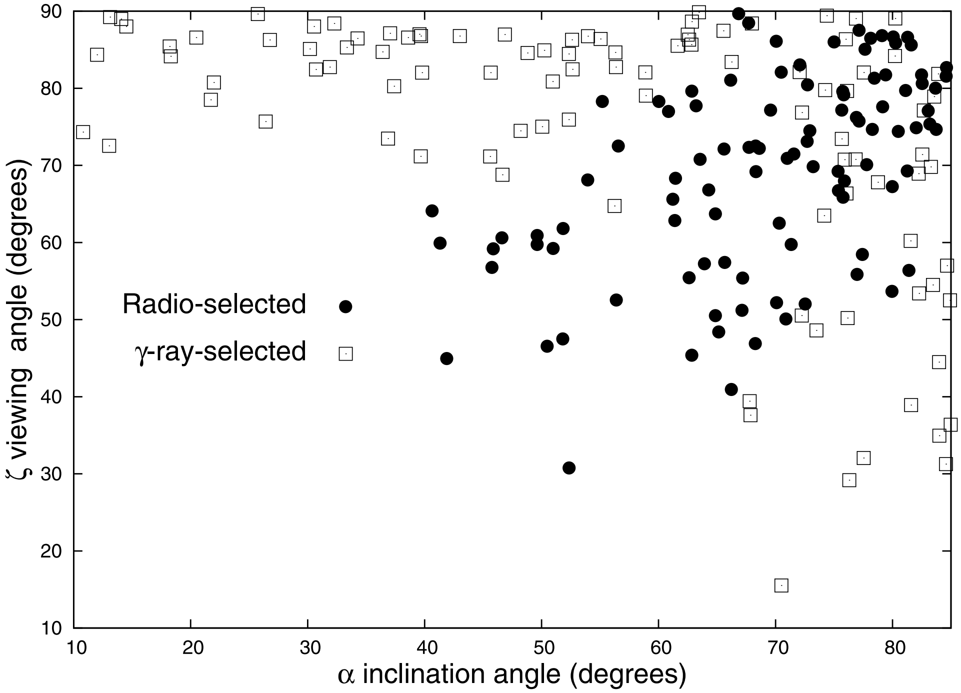

Figure 9. The rotation axis α and viewing angle ζ for the simulated canonical γ-ray pulsars. Filled circles: radio-selected pulsars. Boxes: γ-ray-selected pulsars.

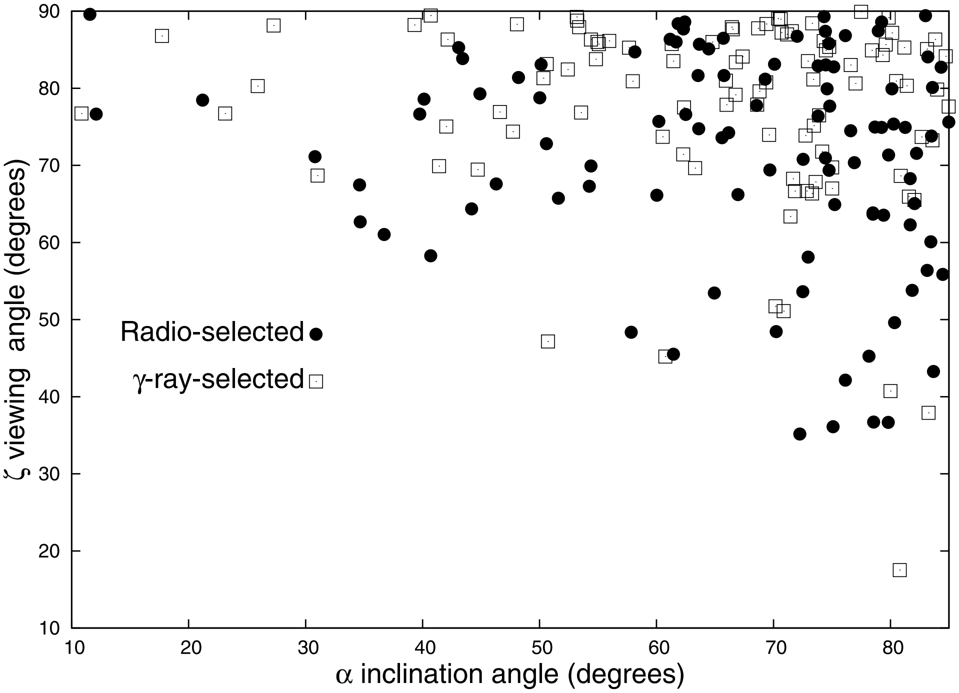

Figure 10. The same as Fig. 9, but for millisecond pulsars.

that the radio-selected and γ-ray-selected pulsars are distributed in different regions in the α– ζ plane. Specifically, the radio-selected CPs group together around the line $\alpha = \zeta$. This is because we have assumed that the magnetic axis is the centre of the radio cone, indicating that the radio emission can be detected by an observer with a viewing angle $\zeta \sim \alpha$. The scattering from the line $\alpha = \zeta$ is related to the width of the radio cone. For example, if we assume a narrower cone than that of equation (15), the amplitude of the scattering is reduced. Fig. 9 also shows that the detected γ-ray pulsars are mainly distributed with a viewing angle $\zeta \sim 70$–90°. These results are consistent with the results of Watters & Romani (2011).

Unlike the case of CPs, the distributions of radio-selected and γ-ray-selected MSPs on the α– ζ plane overlap each other. This is because the width of the radio beam described by equation (16) covers almost the whole sky. We note that most γ-ray-selected MSPs in the simulation irradiate the Earth with radio emission, but the radio fluxes are lower than the sensitivity of the simulated radio surveys (cf. Tables 1 and 2).

In Figs 9 and 10, we can see that no γ-ray pulsars are detected with smaller inclination angles ($\alpha \ll 90^\circ$) and smaller viewing angles ($\zeta \ll 90^\circ$). This is because the γ-ray flux decreases as the viewing angle and/or inclination angle decreases, as discussed in Section 4.1

Table 1. Population of simulated radio-selected (N_{r}) and γ-ray-selected (N_{g}) CPs for six-month, five-year and 10-year *Fermi* observations. First line: the results for 10 radio surveys listed in table 1 of Takata et al. (2010a). Second and third lines: results with sensitivities increased by factors of 2 and 10, respectively. Bottom line: the populations associated with only beaming effects of the radio emission.

	Six-month		Five-year		10-year	
CPs	N_{r}	N_{g}	N_{r}	N_{g}	N_{r}	N_{g}
Ra. Sen. (× 1)	40	39	56	138	59	182
Ra. Sen. (× 2)	51	34	77	123	81	163
Ra. Sen. (× 10)	72	28	130	90	145	120
Beaming	76	28	155	79	177	102

Table 2. The same as Table 1, but for MSPs.

	Six-month		Five-year		10-year	
MSPs	N_{r}	N_{g}	N_{r}	N_{g}	N_{r}	N_{g}
Ra. Sen. (× 1)	10	52	14	200	16	284
Ra. Sen. (× 2)	16	48	26	190	29	274
Ra. Sen. (× 10)	45	32	82	152	94	227
Beaming	106	11	321	41	438	62

(cf. Figs 3 and 4). Hence, our simulation results predict that pulsars with larger inclination and larger viewing angles ($\alpha, \xi \rightarrow 90^{\circ}$) have been preferentially detected by the *Fermi* six-month long observations.

4.2.2 *Population*

Tables 1 and 2 show the simulated populations of CPs and MSPs, respectively, for *Fermi* six-month, five-year and 10-year long observations. Here we scale the sensitivity of the *Fermi* observations as $\propto \sqrt{T}$, where T is the length of the observation time. In addition, the second ('Ra. Sen. (x2)') and third lines ('Ra.Sen. (x10)') in the tables show the results for the 10 radio surveys, but with sensitivities increased by factors of 2 and 10, respectively, and the fourth line ('Beaming') shows the population associated with only the beaming effect of the radio emission.

With the previous radio surveys (first line in Table 1), the present simulation shows that 40 radio-selected and 39 γ-ray-selected CPs can be detected by the *Fermi* six-month observations, indicating that the present model predicts more γ-ray pulsars than the *Fermi* observations ($\sim$20 for both radio-selected and γ-ray-selected γ-ray pulsars). To explain the difference between the simulated and observed numbers, several reasons may be given: (1) the *Fermi* sensitivity will become much worse at the Galactic plane and (2) the γ-ray emission from pulsars may be missed owing to source confusion with complex regions and unresolved sources that are not modelled in the diffuse background. The predicted number (10) of radio-selected γ-ray MSPs is consistent with the observed number (9). The present model predicts that 56 (or 59) radio-selected and 138 (or 182) γ-ray-selected CPs can be detected by *Fermi* with five-year (or 10-year) observations. For the MSPs, 14 (or 16) radio-selected γ-ray pulsars will be detected by *Fermi* with five-year (or 10-year) observations.

We see in the first lines of Tables 1 and 2 that the simulated numbers of radio-selected γ-ray CPs and MSPs increase by only $\sim$20 and $\sim$10 sources, respectively, over even 10-year *Fermi* observations. This implies that most presently known radio pulsars ($\sim$2000 for CPs and $\sim$80 for MSPs) might not be discovered by *Fermi*. For γ-ray-selected pulsars, on the other hand, the simulation predicts that *Fermi* can detect about 140 CPs for about five-year observations. We note that the predicted number of radio-loud (or radio-quiet) γ-ray pulsars really depends on the sensitivity of radio surveys, as Table 1 shows: for example, the predicted number of γ-ray-selected CPs after 10 years of *Fermi* observations decreases from 182 to 120 if the sensitivity of radio surveys increases by a factor of 10. This indicates that a deep radio search may find more radio emission from γ-ray-selected pulsars, such as the LAT PSRs J1741−2054 and J2032+4127 (Camilo et al. 2009). Table 1 also shows that if the sensitivity of radio surveys increases by a factor of 10, the ratio of radio-loud and radio-quiet γ-ray pulsars is almost determined by the beaming effect of the radio emission.

For MSPs (Table 2), most simulated pulsars are categorized as γ-ray-selected pulsars using previous sensitivities of radio surveys, although *Fermi* has not confirmed the radio-quiet MSPs. We argue that it may be difficult to identify radio-quiet MSPs, because the detection of the rotation period by a *Fermi* blind search is much harder than for CPs. Furthermore, if an MSP is in a binary system, the effects of orbital motion on the observed rotation period make it even harder to confirm a millisecond rotation period by a blind search. Takata et al. (2011b) discussed the idea that the γ-ray-selected MSPs in the simulation correspond to the *Fermi* unidentified sources located at higher Galactic latitudes.

We note that the radio cones from MSPs are quite huge, so that most MSPs irradiate the Earth with radio emission, as the bottom line in Table 2 shows. This implies that more radio MSPs associated with *Fermi* unidentified sources will be detected by future radio surveys, such as the discovery of 20 new radio MSPs associated with *Fermi* unidentified sources (Caraveo 2010; Keith et al. 2011; Ransom et al. 2011; Ray & Saz Parkinson 2011). As the third line in Table 2 shows, however, even if we drastically increase the radio sensitivity by a factor of 10, so that the number of radio-selected MSPs detected by 10-year *Fermi* observations can increase from 16 to 94, the number is still much lower than the expected 227 γ-ray-selected millisecond pulsars. Unless the *Fermi* sensitivity of the blind search is improved, most γ-ray MSPs will not be identified and will contribute to *Fermi* unidentified sources and/or the γ-ray background radiation.

4.2.3 *γ-ray radiation characteristics*

Figs 11-13 show the radiation characteristics (γ-ray luminosity, cut-off energy and photon index, respectively) versus other characteristics (spin-down power or magnetic field strength at the light cylinder) for γ-ray pulsars with six-month observations. In these figures, we plot the *Fermi* data with errors taken from Abdo et al. (2010a) and Saz Parkinson et al. (2010) and present the simulated pulsars in the subfigures. For the simulated pulsars, we randomly choose 200 simulated γ-ray pulsars (except for the γ-ray-selected MSPs).

In Fig. 11, the γ-ray luminosity is calculated from $L_{\gamma} = 4\pi d^2 F_{\gamma,100}$, where d is the distance, and histograms of the values of γ-ray luminosity are projected along the right-hand axis. The solid and dashed histograms represent the distributions for simulated and observed γ-ray pulsars, respectively. The present model predicts that most γ-ray CPs have a spin-down power of $L_{\rm sd} \sim 10^{35-38}\,{\rm erg\,s^{-1}}$ and a γ-ray luminosity of $L_{\gamma} \sim 10^{34-36}$, while MSPs have $L_{\rm sd} \sim 10^{33-35}\,{\rm erg\,s^{-1}}$ and $L_{\gamma} \sim 10^{32.5-34.5}\,{\rm erg\,s^{-1}}$, consistent with the *Fermi* observations.

In Fig. 11, the spin-down power $L_{\rm sd}$ and γ-ray luminosity L_{γ} of the simulated pulsars can be related as $L_{\gamma} \propto L_{\rm sd}^{\beta}$ with $\beta \sim 0$ for $L_{\rm sd} \geq 10^{35-36}\,{\rm erg\,s^{-1}}$ and $\beta \sim 0.5$ for $L_{\rm sd} \leq 10^{35-36}\,{\rm erg\,s^{-1}}$. In the present emission model, the γ-ray luminosity is proportional to $L_{\gamma} \propto f^3 L_{\rm sd}$, as Figs 3 and 4 indicate (cf. Takata et al. 2011b). The change of slope is caused by switching the gap-closure process between the photon–photon pair-creation process and the magnetic pair-creation process. As equations (32)-(34) show, the gap fraction depends on the rotation period and the magnetic field as $f_{\rm zc} \propto P^{26/21} B^{-4/7}$ for the photon–photon pair-creation process and $f_{\rm m} \propto P^{1/2}$ for the magnetic pair-creation process. These relations imply that the γ-ray luminosity depends on the spin-down power as $L_{\gamma} \propto L_{\rm sd}^{1/14}$ for the photon–photon pair-creation process and $L_{\gamma} \propto L_{\rm sd}^{5/8}$ for the magnetic pair-creation process. Equating $f_{\rm zc}$ (32) and $f_{\rm m}$ (34) corresponds to $L_{\rm sd} \sim 10^{35-36}\,{\rm erg\,s^{-1}}$. The change of slope

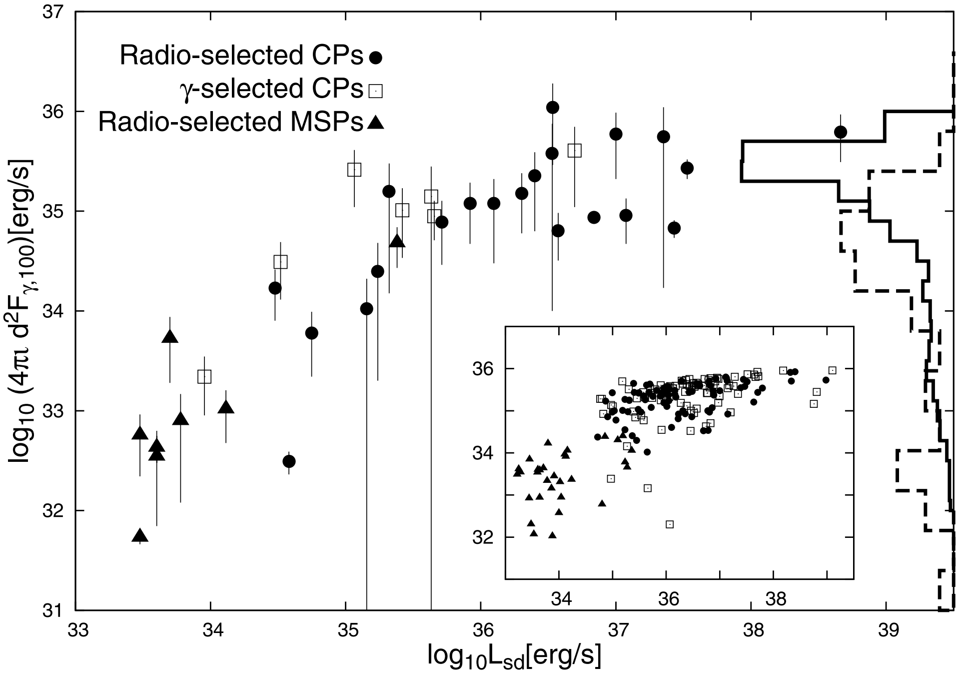

Figure 11. The γ-ray luminosity, $L_\gamma = 4\pi d^2 F_{\gamma,100}$, versus the spin-down luminosity, $L_{\rm sd}$, as result of a six-month long observation. *Fermi* data with errors are taken from Abdo et al. (2010a) and Saz Parkinson et al. (2010) and the 200 samples of simulated pulsars are plotted in the inset. Filled circles: radio-selected CPs. Squares: γ-ray-selected CPs. Filled triangles: radio-selected MSPs. Histograms of the values of γ-ray luminosity are projected along the right-hand axis. The solid and dashed histograms are results for simulated and observed pulsars, respectively.

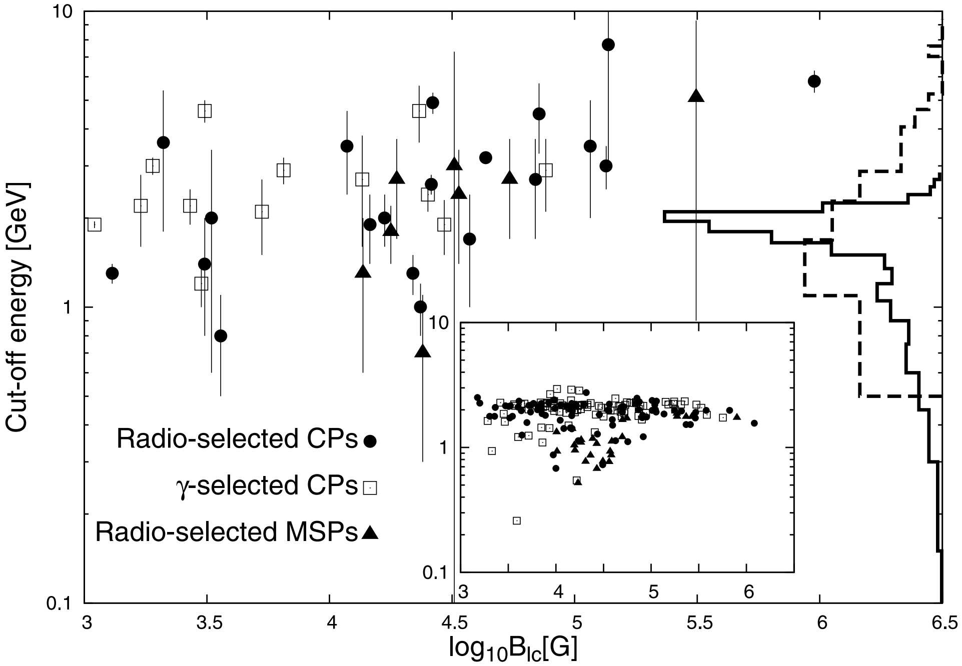

Figure 12. The cut-off energy versus the magnetic field at the light cylinder, $B_{\rm lc}$. The symbols and histograms correspond to the same cases as Fig. 11.

β has been found by Wang et al. (2010), who used the two-layer outer-gap model to fit the phase-averaged spectrum of mature γ-ray pulsars observed by *Fermi*.

Although the general trend of the relation between γ-ray luminosity and spin-down power is explained with a simple form $L_\gamma \propto L_{\rm sd}^{\beta}$, we can see in Fig. 11 that some simulation samples deviate from the relation. For example, some simulated pulsars with a spin-down power of $L_{\rm sd} \sim 10^{36}$ erg s^{-1} have a γ-ray luminosity of $L_\gamma \sim 10^{32-33}$ erg s^{-1}, which is about two or three orders smaller than the typical value of $L_\gamma \sim 10^{35}$ erg s^{-1}. We emphasize that this low efficiency of γ-ray emission is mainly caused by the effects of viewing angle. Pulsars lying on the relation $L_\gamma \propto L_{\rm sd}^{\beta}$ are observed with viewing angles of $\zeta \sim 90°$, whereas those (‘apparently’) low-efficiency γ-ray pulsars are observed with

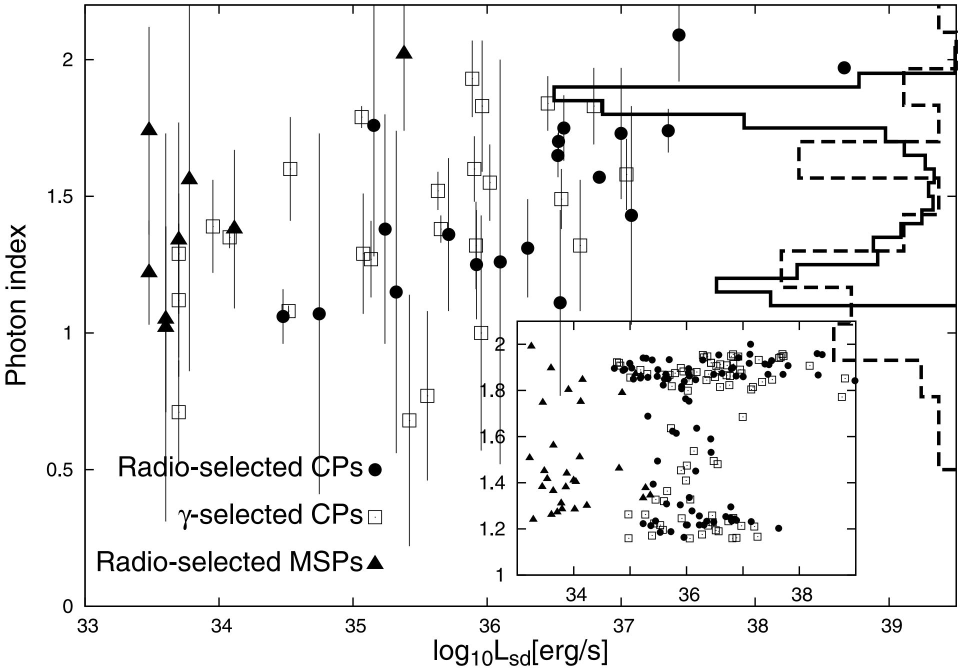

Figure 13. The photon index versus the spin-down luminosity. The symbols and histograms correspond to the same cases as Fig. 11.

smaller viewing angles. The flux is more sensitive to the viewing angle than the inclination angle, although it also depends on the latter, as Figs 3 and 4 show. We note that lower efficiency γ-ray pulsars tend to be located closer to Earth.

Fig. 12 shows the cut-off energy versus the magnetic field at the light cylinder, $B_{\rm lc}$. The symbols and the histograms correspond to the same cases as Fig. 11. As the inset in Fig. 12 indicates, the present simulation predicts that most γ-ray CPs and MSPs have magnetic fields at the light cylinder of $B_{\rm lc} \geq 10^3$ G and $B_{\rm lc} \geq 10^4$ G, respectively, and a cut-off energy smaller than $\sim$2 GeV. These features are consistent with the *Fermi* observations. In the figure, some simulated CPs have a cut-off energy significantly smaller than the typical value $E_{\rm c} \sim 2$ GeV. As in the case of γ-ray luminosity, this deviation from the typical value is caused by the effects of viewing angle, as Figs 5 and 6 imply. In Fig. 12, our simulation predicts that the typical cut-off energy (1–1.5 GeV) of MSPs is smaller than that ($\sim$2 GeV) of CPs. It is difficult to discuss the difference in the observed cut-off energies between CPs and MSPs, because of the large observational errors.

Fig. 13 represents the photon index versus the spin-down power. We can find that the model distribution of the photon index has two peaks at $p \sim 1.2$–1.3 and $p \sim 1.8$–2, and the observed distribution (dashed histogram) may also have two peaks at $p \sim 1.3$ and $p \sim 1.7$. With the present model, the hard component of $p \sim 1.2$–1.3 corresponds to the spectrum associated with emission from only the main acceleration region, while the soft component $p \sim 1.8$–2 corresponds to the spectrum composed of emission from both main and screening regions, as we discussed in Section 4.1.3. The present model does not predict a very hard spectrum with index $p \leq 1$, which has been indicated for some *Fermi* pulsars.

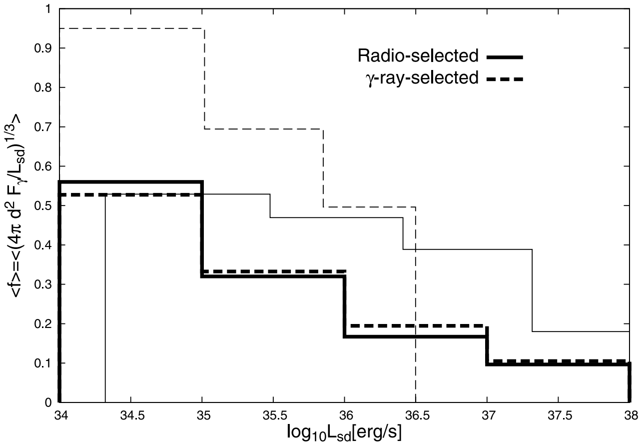

Figure 14. Averaged value of the *observed* fractional gap thickness, $f_{\rm o} \equiv (4\pi d^2 F_\gamma / L_{\rm sd})^{1/3}$, of the detected γ-ray pulsars as a function of the spin-down power. The solid and dashed histograms show the results of radio-selected and γ-ray-selected pulsars, respectively. The thick and thin lines correspond to the simulation and *Fermi* observation, respectively.

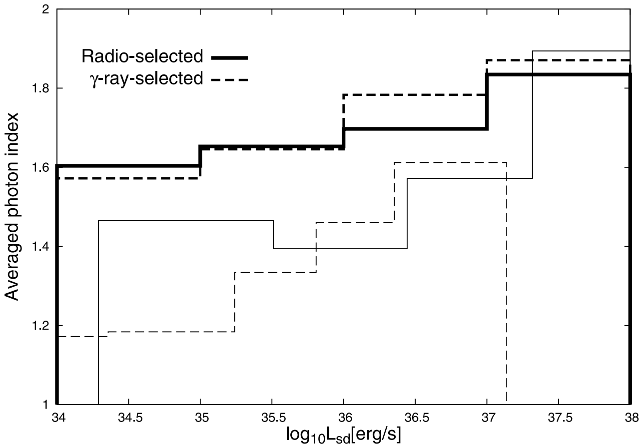

Figure 15. Averaged value of the photon index of the detected γ-ray pulsars as a function of the spin-down power. The histograms correspond to the same cases as Fig. 14.

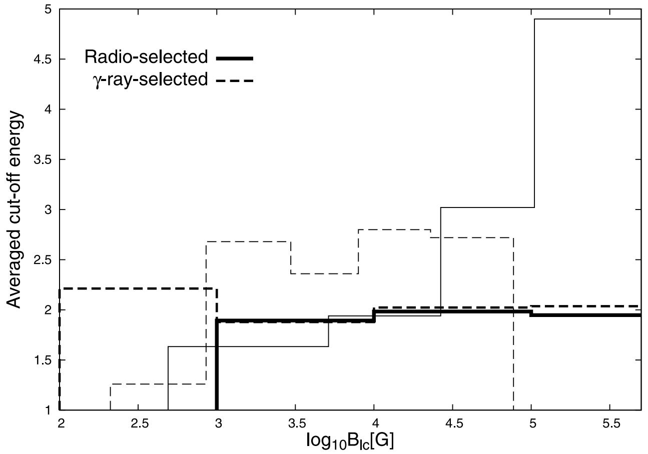

Figure 16. Averaged value of the cut-off energy of the detected γ-ray pulsars as a function of the spin-down power. The histograms correspond to the same cases as Fig. 14.

Figs 14 and 15 represent the averaged *apparent* fractional thickness, which is defined by $f_{\rm a} \equiv (4\pi d^2 F_\gamma / L_{\rm sd})^{1/3}$, and the photon index, respectively, as a function of the spin-down power, and Fig. 16 shows the averaged cut-off energy as a function of the magnetic field at the light cylinder. In the figures, the solid and dashed lines represent the results for radio-selected and γ-ray-selected CPs, respectively. In addition, the thick and thin lines correspond to the results of the simulation and *Fermi* observations, respectively. In Fig. 14, our model predicts a tendency that the apparent fractional thickness, $f_{\rm a}$, tends to decrease with the increase of spin-down power. This is because the *true* fractional thickness, $f_{\rm zc}$ or $f_{\rm m}$, tends to decrease with the increase of spin-down power, i.e. $f_{\rm zc} \propto L_{\rm sd}^{-13/21} B^{1/21}$ from equation (32) and $f_{\rm m} \propto L_{\rm sd}^{-1/8} B^{1/4}$ from equation (34). Because the photon index of the spectrum tends to increase with the decrease fractional gap thickness, as Fig. 7 shows, the averaged photon index in Fig. 15 increases with spin-down power. We find that this behaviour is qualitatively consistent with the *Fermi* observations. In Fig. 16, our model predicts that the typical cut-off energy does not depend much on the magnetic field strength at the light cylinder, while the present *Fermi* data may show a tendency for the cut-off energy to increase with magnetic field strength at the light

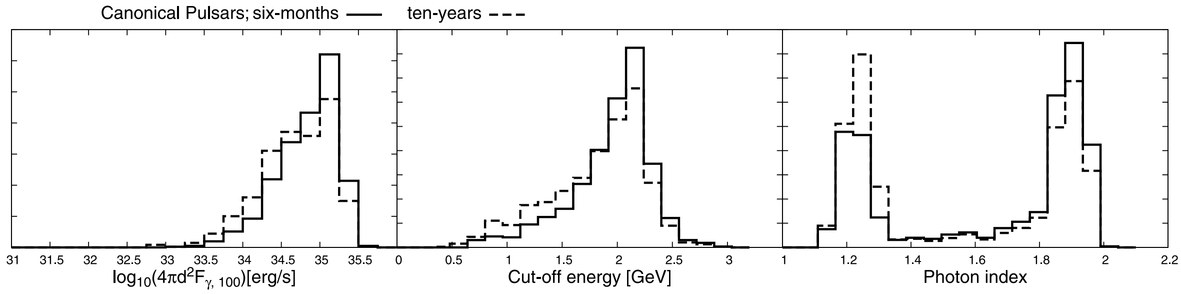

Figure 17. Simulated distributions for canonical pulsars. Left: luminosity. Middle: cut-off energy. Right: photon index. The solid and dashed lines are results for simulated six-month and 10-year *Fermi* observations, respectively.

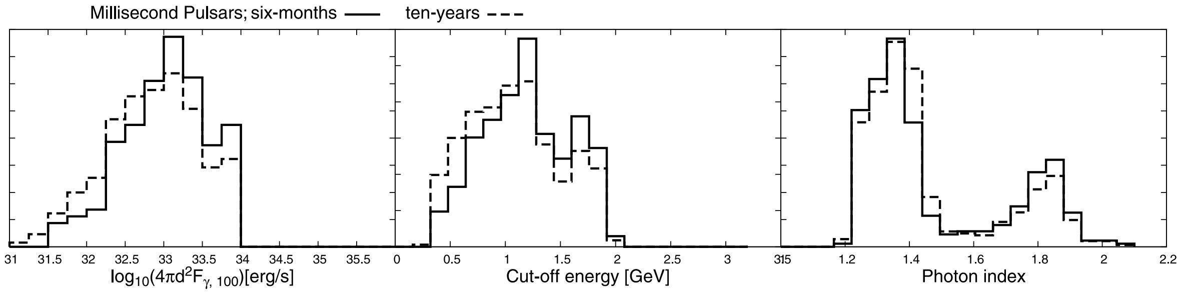

Figure 18. The same as Fig. 17, but for millisecond pulsars.

cylinder. However, because the observational errors are so large, a deeper observation to reduce the errors may be required in order to discuss this tendency.

In Figs 17 and 18 we summarize the distribution of radiation characteristics for the simulated canonical and millisecond γ-ray pulsars, respectively, including both radio-selected and γ-ray-selected pulsars. The solid and dashed lines are results for the simulated six-month and 10-year *Fermi* observations, respectively. Comparing the solid and dashed lines, we find that the distributions do not depend much on the time span of the *Fermi* observations. However, we note that a longer observation enables us to detect γ-ray pulsars with smaller fluxes, which include γ-ray pulsars with a viewing angle close to the rotation axis (cf. Figs 3 and 4). For an observer with a viewing angle close to the rotation axis, the photon index tends to be $p \sim 1.2$–1.3, as Figs 7 and 8 show. Therefore, our model prediction is that a longer *Fermi* observation will detect more γ-ray pulsars with photon indexes $p \sim 0.12$–0.14, as the right panels in Figs 17 and 18 indicate.

4.2.4 *Pulse profiles*

Figs 19–22 present calculated pulse profiles for different types of γ-ray pulsar. For each type of γ-ray pulsar, 64 samples are randomly chosen to present the model predictions on the statistical distribution of the morphology of the pulse profiles. From left to right and from the top

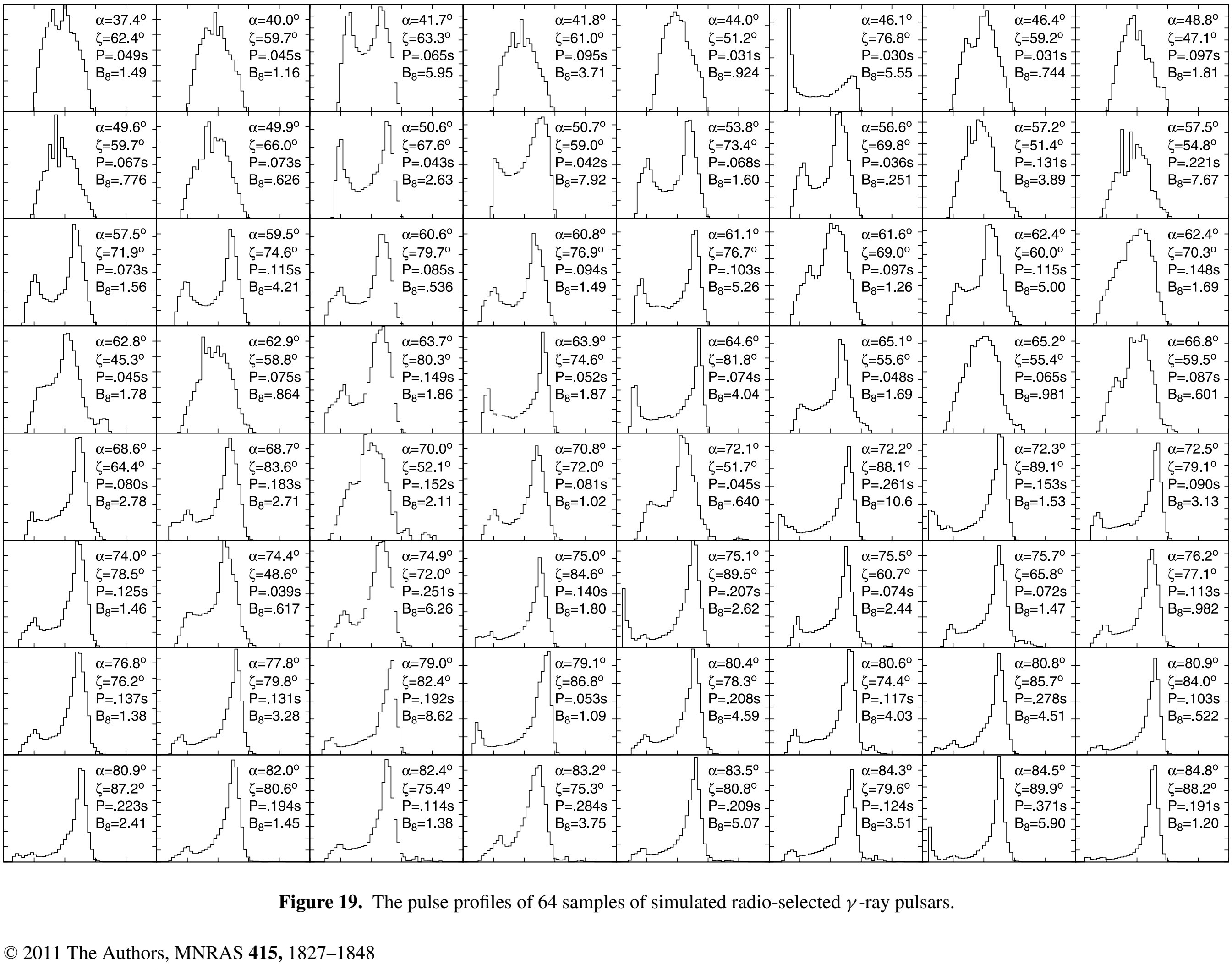

Figure 19. The pulse profiles of 64 samples of simulated radio-selected γ-ray pulsars.

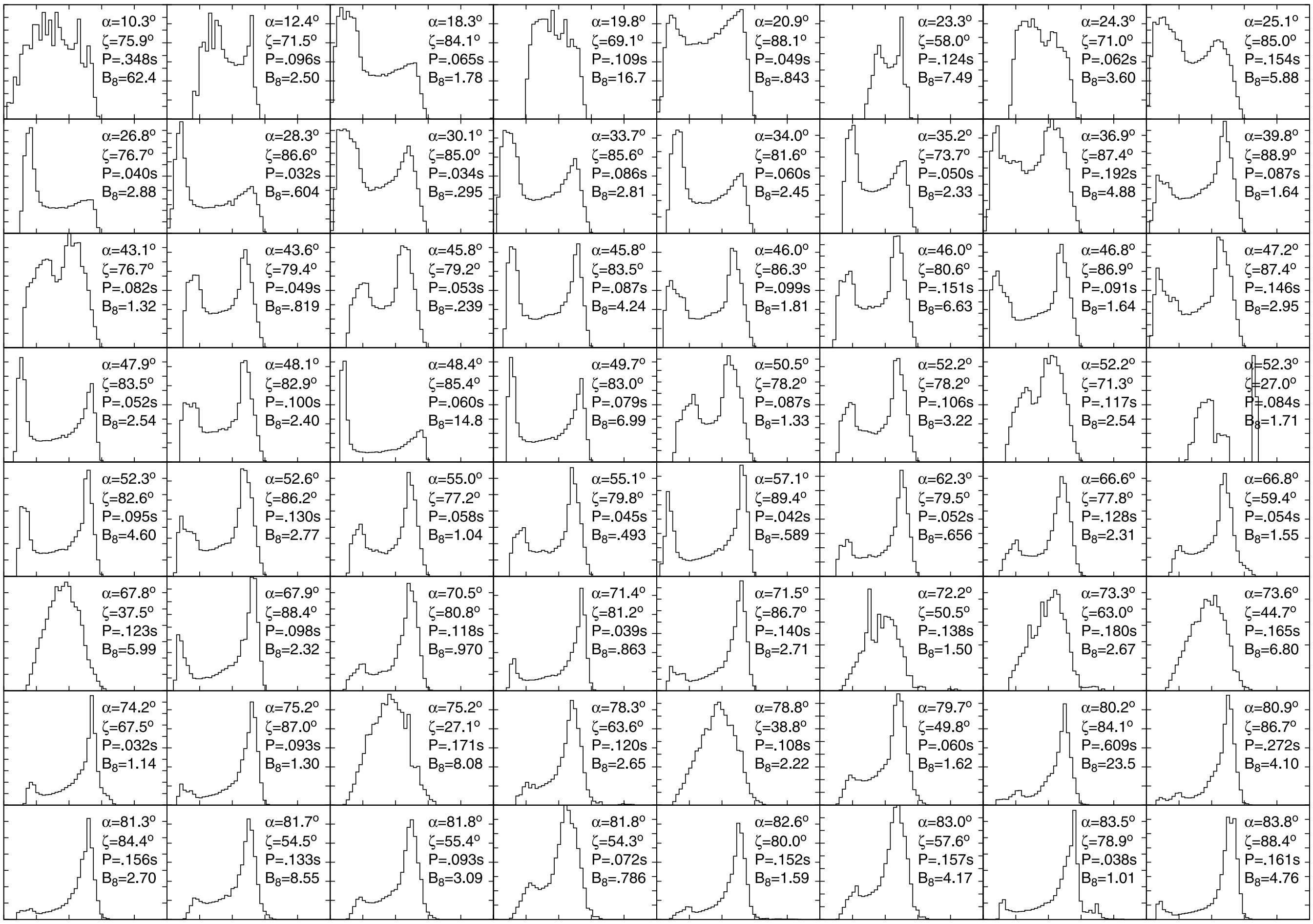

Figure 20. The pulse profiles of 64 samples of simulated γ-ray-selected canonical pulsars.

to bottom in the figures, the inclination angle increases. In principle, we can quantitatively compare the simulated morphology of the pulse profiles in Figs 19–22 (e.g. phase-separation, number of peak) with *Fermi* observations. However, we would like to point out that it is very difficult to quantify the morphology in order to compare with the observations. In Fig. 19, for example, the pulse profile represented in the upper left conner is indeed a double-peak structure with narrow phase-separation between the two peaks. In the observations, however, the identification of a double-peak structure with such a narrow peak separation really depends on the source counts and timing ephemerides of the pulsars. In Fig. 20, the simulated pulse profile presented in the seventh line and first column ($\alpha = 74\overset{\circ}{.}2$ and $\zeta = 67\overset{\circ}{.}5$) has a first peak much smaller than the second peak. In the observations, the detection of such a small peak will depend on the strength of the background radiation. Moreover, because the intensity of the pulse peak will depend on the modelling of the gap structure, it is difficult to discuss the distribution of the intensity ratio of first and second peaks with the present simple three-dimensional model. In the present paper, therefore, we avoid a quantitative discussion regarding the morphology of the pulsed profile. Instead, we can only present a qualitative comparison.

We note that the peaks emerging in the calculated pulse profiles are caused by the so-called caustic effect (Romani & Yadigaroglu 1995; Cheng, Ruderman & Zhang 2000; Dyks, Rudak & Harding 2004), in which more photons are observed at narrow width of the rotation phase due to special-relativistic effects, i.e. the aberration of the emission direction and photon travel time. In such a case, the pulse phase and the number of the main peak are not affected much by modelling of the gap structure, whereas the intensity of the peak depends on the gap structure.

We can see in Figs 19 and 20 that the pulse profiles of the simulated CPs (in particular, γ-ray-selected CPs) are described by a double-peak structure rather than a single-peak profile. This result may explain the tendency for most canonical γ-ray pulsars observed by *Fermi* to show a double-peak structure. In the present simulations, we have predicted that γ-ray pulsars measured from $\zeta \sim 90^\circ$ are preferentially detected in the simulation (cf. Section 4.1). With viewing angles closer to $\zeta \sim 90^\circ$, the calculated pulse profile tends to have a double-peak structure.

For radio-selected canonical γ-ray pulsars, although the double-peak structure is a more or less common feature, single-pulse structures or double-peak structures with a narrow phase separation are notable for pulsars with inclination angles $\alpha \sim 40^\circ$–50°, as we can see in Fig. 19. This is because the simulated radio-selected canonical pulsars have a viewing angle similar to the inclination angle (cf. Fig. 9), $\zeta \sim \alpha$. With the present outer-gap geometry, the pulse profile for a smaller viewing angle ($\zeta \ll 90^\circ$) tends to have a single peak or a double peak with narrow phase separation, as the phase plot of Fig. 2 shows.

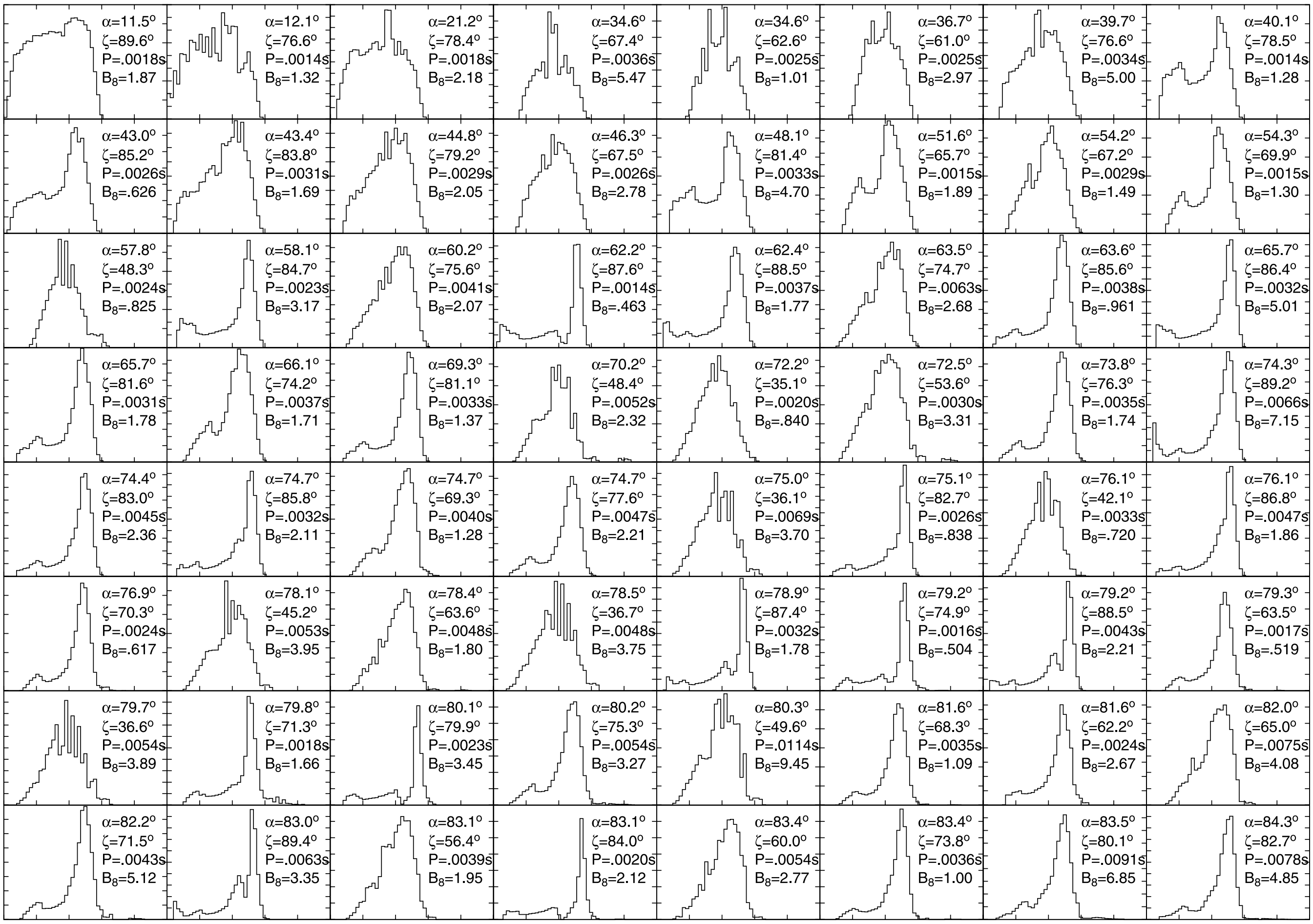

Figure 21. The pulse profiles of 64 samples of simulated radio-selected millisecond γ-ray pulsars.

Comparing the pulse profiles of CPs (Figs 19 and 20) and MSPs (Figs 21 and 22), one sees that pulse profiles with a single peak are more common for MSPs than for CPs. In the present model, the fractional gap thickness $f_{\rm zc,MSP}$ of equation (33) for the MSPs tends to be larger than $f_{\rm zc,CP}$ of equation (32) for the CPs. With a larger fractional gap thickness, the emission from higher altitudes (larger z in units of the light radius) contributes to the pulse profile. Because the emission from higher altitudes produces two caustic peaks with a narrower phase separation, the calculated pulse profiles of MSPs have single-peak or double-peak structures with narrow phase separation in more cases than CPs.

5 SUMMARY AND DISCUSSION

In this paper, we have applied the so-called two-layer outer-gap model for γ-ray radiation from pulsars, and have focused on the dependence of the γ-ray radiation characteristics on the inclination and viewing angles. We showed that the γ-ray flux and spectral cut-off energy decrease as the viewing angle deviates from $\zeta = 90^\circ$. The spectrum above 100 MeV becomes soft with a photon index $p \sim 1.8$–2 for an observer with a large viewing angle ($\zeta \rightarrow 90^\circ$), whereas it becomes hard with a index $p \sim 1.2$–1.3 for an observer with a smaller viewing angle ($\zeta \ll 90^\circ$). The spectrum with photon index $p \sim 1.8$–2 consists of emission from both main acceleration and screening regions, while $p \sim 1.2$–1.3 corresponds to emission from only the main acceleration region.

We have developed a Monte Carlo simulation for the population of γ-ray-emitting pulsars. Our simulation predicts that 56 (or 59) radio-selected pulsars, 138 (or 182) γ-ray-selected canonical γ-ray pulsars and 14 (or 16) radio-selected γ-ray MSPs can be detected by five-year (or 10-year) *Fermi* observations. Even if we drastically increase the radio sensitivity by a factor of 10, most simulated MSPs are expected in the form of γ-ray-selected MSPs, which will contribute as *Fermi* unidentified sources and/or γ-ray background radiation. For the viewing geometry, our simulation predicts that radio-selected CPs have inclination angle (α) and viewing angle (ζ) of $\alpha \sim \zeta$, and that most γ-ray pulsars detected by *Fermi* have been measured with a viewing angle of $\zeta = \sim 70^\circ$–90°. We demonstrated that the spin-down power $L_{\rm sd}$ and γ-ray luminosity L_γ of the simulated pulsars are related as $L_\gamma \propto L_{\rm sd}^\beta$ with $\beta \sim 0$ for $L_{\rm sd} \geq 10^{35-36}\,{\rm erg\,s^{-1}}$ and $\beta \sim 0.5$ for $L_{\rm sd} \leq 10^{35-36}\,{\rm erg\,s^{-1}}$. The change of the slope β is associated with the switching of the gap-closure mechanism from the photon–photon pair-creation process of $L_{\rm sd} \geq 10^{35-36}\,{\rm erg\,s^{-1}}$ to the magnetic pair-creation process of $L_{\rm sd} \leq 10^{35-36}\,{\rm erg\,s^{-1}}$. We showed that the distribution of the photon index of the simulated γ-ray pulsars has two peaks at $p \sim 1.8$–2 and $p \sim 1.2$–1.3, which may explain the observed distribution. We

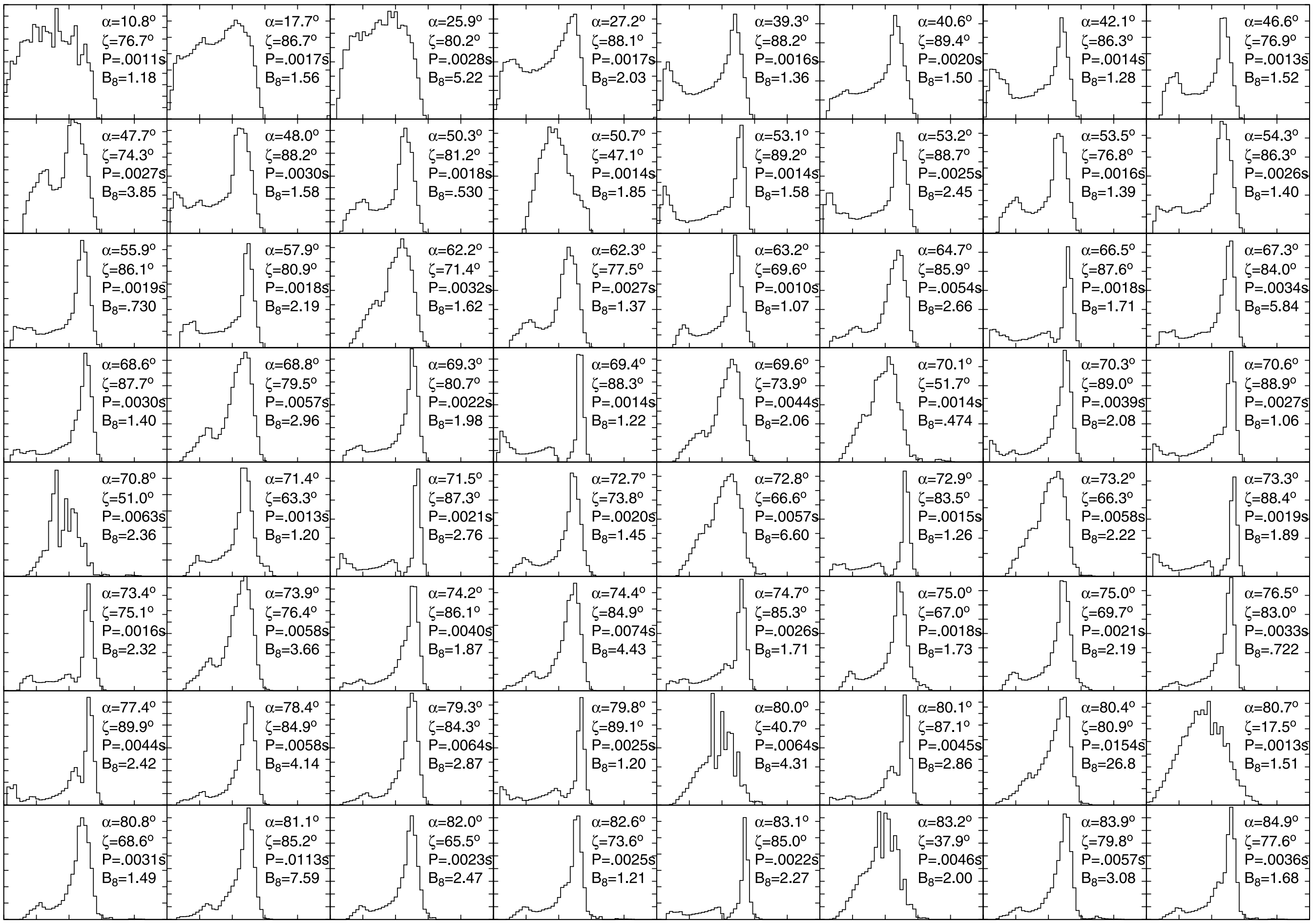

Figure 22. The pulse profiles of 64 samples of simulated γ-ray-selected millisecond pulsars.

expect that more γ-ray pulsars with a hard spectrum of $p \sim 1.2$–1.3 will be detected by future *Fermi* observations. For the pulse profiles, the present simulation explains the observational tendency that most canonical γ-ray pulsars detected by *Fermi* have pulse profiles with double peaks. Our model suggests that a single-pulse profile or a double-pulse profile with a narrower phase separation is more common for MSPs than CPs.

The present model can be used to diagnose the viewing geometry of γ-ray pulsars. For example, the present model predicts that most present γ-ray pulsars detected by *Fermi* will have viewing angle $\zeta \sim 70^\circ$–90°, and hence a pulse profile with double peaks is more common than one with a single peak. On the other hand, we expect that PSR J0659+1414, which is known as an extremely low-efficiency γ-ray pulsar (Abdo et al. 2010c), has a unique viewing geometry. PSR J0659+1414 is a radio-loud γ-ray pulsar and its spin-down power is $L_{\rm sd} = 3 \times 10^{34}\,{\rm erg\,s^{-1}}$. Interestingly, the γ-ray emission from PSR J0659+1414 has been observed with a γ-ray luminosity $L_\gamma \sim 3 \times 10^{32}\,{\rm erg\,s^{-1}}$, which is about two orders smaller than the typical value for pulsars with a similar spin-down power. To explain the observed low efficiency of γ-ray radiation, our simulation predicts that the inclination angle and viewing angle are relatively small, say $\alpha \sim \zeta \sim 40^\circ$–$50^\circ$, and hence the apparent efficiency is significantly reduced from the typical value (cf. Fig. 3). For PSR J0659+1414 it is also known that the spectral cut-off energy, $E_{\rm c} \sim 0.7$ GeV, is suggestively smaller than the typical value of $E_{\rm c} \sim 2$ GeV. This behaviour can also be explained by the effects of the viewing geometry, as Fig. 5 indicates. Furthermore, our simulation suggests that pulsars measured as low-efficiency γ-ray pulsars are located closer to Earth. In fact, PSR J0659+1414 with $d \sim 0.28$ kpc is one of the nearest γ-ray pulsars. Finally, the observed broad single-pulse profile of PSR J0659+1414 is also expected from the present calculation. As discussed in Section 4.2.4 (Fig. 19), a single-pulse structure or double-peak structure with a narrow phase separation is more common for radio-selected canonical γ-ray pulsars with inclination angle $\alpha \sim 40^\circ$–50°. On these grounds, the unique radiation properties of PSR J0659+1414 can be explained if *Fermi* has measured the γ-ray emission from outer-gap with the viewing geometry $\alpha \sim \zeta \sim 40^\circ$–$50^\circ$. It is expected that the population of low-efficiency γ-ray pulsars will be increased by future *Fermi* observations. The diagnosis of γ-ray efficiency, pulse profile and cut-off energy will provide a strong constraint on emission models.

ACKNOWLEDGMENTS

We thank A.H. Kong, C.Y. Hui, B. Rudak, Lupin-C.C. Lin, M. Ruderman, R.E. Taam and S. Shibata for useful discussions. We express our appreciation to an anonymous referee for useful comments. We also thank the Theoretical Institute for Advanced Research in Astrophysics (TIARA) operated under the Academia Sinica Institute of Astronomy and Astrophysics, Taiwan, which enabled one author (JT) to use the PC cluster at TIARA. KSC is supported by a 2011 GRF grant of the Hong Kong SAR Government entitled 'Gamma-ray Pulsars'.

REFERENCES

Abdo A. A. et al., 2009a, Sci., 325, 840
Abdo A. A. et al., 2009b, Sci., 325, 848
Abdo A. A. et al., 2009c, ApJ, 706, 1331
Abdo A. A. et al., 2010a, ApJS, 187, 460
Abdo A. A. et al., 2010b, ApJS, 188, 405
Abdo A. A. et al., 2010c, ApJ, 708, 1426
Abdo A. A. et al., 2010d, ApJ, 712, 957
Aliu E. et al., 2008, Sci, 322, 1221
Arons J., 1983, ApJ, 266, 215
Bailes M., Kniffen D. A., 1992, ApJ, 391, 659
Binney J. J., Tremaine S. D., 1987, Galactic Dynamics. Princeton Univ. Press, Princeton
Burton W. B., Gordon M. A., 1978, A&A, 63, 7
Camilo F. et al., 2009, ApJ, 705, 1
Campana S., Colpi M., Mereghetti S., Stella L., Tavani M., 1998, A&AR, 8, 279
Caraveo P. A., 2010, in Proc. Sci., High Time Resolution Astrophysics (HTRA) IV. SISSA, Trieste (arXiv:1009.2421)
Cheng K. S., Zhang L., 1998, ApJ, 498, 327
Cheng K. S., Ho C., Ruderman M., 1986a, ApJ, 300, 500
Cheng K. S., Ho C., Ruderman M., 1986b, ApJ, 300, 522
Cheng K. S., Ruderman M., Zhang L., 2000, ApJ, 537, 964
Cordes J. M., Lazio T. J. W., 2002, preprint (astro-ph/0207156)
Daugherty J. K., Harding A. K., 1982, ApJ, 252, 337
Daugherty J. K., Harding A. K., 1996, ApJ, 458, 278
Davis L., Goldstein M., 1970, ApJL, 159, 81
Dyks J., Rudak B., Harding A. K., 2004, ApJ, 607, 939
Faucher-Giguère C.-A., Kaspi V. M., 2006, ApJ, 643, 332
Faucher-Giguère C.-A., Loeb A., 2010, J. Cosmol. Astropart. Phys., 1, 5
Goldreich P., Julian W. H., 1969, ApJ, 157, 869
Goldreich P., Reisenegger A., 1992, ApJ, 395, 250
Gonthier P. L., Ouellette M. S., Berrier J., O'Brien S., Harding A. K., 2002, ApJ, 565, 482
Harding A. K., Muslimov A. G., 2011, ApJL, 726, 10
Harding A. K., Stern J. V., Dyks J., Frackowiak M., 2008, ApJ, 680, 1378
Hirotani K., 2006, ApJ, 652, 1475
Hirotani K., 2008, ApJL, 688, 25
Hobbs G., Lorimer D. R., Lyne A. G., Kramer M., 2005, MNRAS, 360, 974
Hoyos J., Reisenegger A., Valdivia J. A., 2008, A&A, 487, 789
Kaaret P., Cottam J., 1996, ApJL, 462, 35
Kaspi V. M., Roberts M. E., Vasisht G., Gotthelf E. V., Pivovaroff M., Kawai N., 2001, ApJ, 560, 371
Keith M. J. et al., 2011, MNRAS, 414, 1292
Kijak J., Gil J., 1998, MNRAS, 299, 855
Kijak J., Gil J., 2003, A&A, 397, 969
Kramer M., Xilouris K. M., 2000, in Kramer M., Wex N., Wielebinski R., eds, IAU Colloq. 177, Pulsar Astronomy 2000 and Beyond. Astron. Soc. Pac., San Francisco, p. 229
Kramer M., Xilouris K. M., Jessner A., Lorimer D. L., Wielebinski R., Lyne A. G., 1997, A&A, 322, 846
Kramer M., Xilouris K. M., Lorimer D. R., Doroshenko O., Jessner A., Wielebinski R., Wolszczan A., Camilo F., 1998, ApJ, 501, 270
Lorimer D. R., 2008, Living Rev. Relativ., 11, 8
Lorimer D. R. et al., 1995, ApJ, 439, 933
Lyne A. G., Graham-Smith F., 2006, eds, Pulsar Astronomy, 3rd edn, Cambridge Astrophysics Series. Cambridge Univ. Press, Cambridge, p. 264
Manchester R. N., Hobbs G. B., Teoh A., Hobbs M., 2005, AJ, 129, 1993 (astro-ph/0412641)
Marshall F. E., Gotthelf E. V., Zhang W., Middleditch J., Wang Q. D., 1998, ApJL, 499, 179
Michel F. C., 1991, Theory of Neutron Star Magnetospheres. Univ. Chicago Press, Chicago
Muslimov A. G., Harding A. K., 2004, ApJ, 617, 471
Narayan R., Ostriker J. P., 1990, ApJ, 352, 222
Paczynski B., 1990, ApJ, 348, 485
Ransom S. M. et al., 2011, ApJL, 727, 16
Ray P. S., Saz Parkinson P. M., 2011, in Rea N., Torres D. F., eds, High-Energy Emission from Pulsars and Their Systems. Springer, Berlin, p. 37
Romani R. W., Watters K. P., 2010, ApJ, 714, 810
Romani R. W., Yadigaroglu I.-A., 1995, ApJ, 438, 314
Romanova M. M., Ustyugova G. V., Koldoba A. V., Lovelace R. V. E., 2009, MNRAS, 399, 1802

Ruderman M. A., Sutherland P. G., 1975, ApJ, 196, 51
Saz Parkinson P. M. et al., 2010, ApJ, 725, 571
Spitkovsky A., 2006, ApJL, 648, 51
Story S. A., Gonthier P. L., Harding A. K., 2007, ApJ, 671, 713
Sturner S. J., Dermer C. D., 1996, A&AS, 120, 99
Takata J., Shibata S., Hirotani K., 2004, MNRAS, 354, 1120
Takata J., Chang H.-K., Cheng K. S., 2007, ApJ, 656, 1044
Takata J., Wang Y., Cheng K. S., 2010a, ApJ, 715, 1318
Takata J., Cheng K. S., Taam R. E., 2010b, ApJL, 723, 68
Takata J., Wang Y., Cheng K. S., 2011a, ApJ, 726, 44
Takata J., Wang Y., Cheng K. S., 2011b, MNRAS, 414, 2173
Tauris T. M., Manchester R. N., 1998, MNRAS, 298, 625
Venter C., Harding A. K., Guillemot L., 2009, ApJ, 707, 800
Wang Y., Takata J., Cheng K. S., 2010, ApJ, 720, 178
Wang Y., Takata J., Cheng K. S., 2011, MNRAS, 414, 2664
Watters K. P., Romani R. W., 2011, ApJ, 727, 123
Yadigaroglu I. A., 1997, PhD thesis, Stanford Univ.
Zhang L., Cheng K. S., 1997, ApJ, 487, 370
Zhang L., Cheng K. S., 2003, A&A, 398, 639

This paper has been typeset from a TEX/LATEX file prepared by the author.